Far-field plume diagnostic of the 100 W-class ISCT100-v2 Hall thruster

IEPC-2019-617

Presented at the 36th International Electric Propulsion Conference
University of Vienna, Austria
September 15-20, 2019

T. Hallouin*, S. Mazouffre† and M. Inchingolo‡
Centre National de la Recherche Scientifique, Orléans, Loire, 45000, France

and

A. Gurciullo§,P. Lascombes¶,J.-L Maria‖
Exotrail, Massy, Essone, 91300, France

The 100 W-class ISCT100-v2 Hall thruster has been characterized with respect toin terms of far-field plume properties. By means of a Faraday Cup and a Retarding Potential Analyzer, both the ion current density and the ion energy distribution function have been measured over a 180° circular arc for different operating points. Measurements are compared to far-field plume characterizations performed with high power Hall thruster, namely the 1.5 kW-class SPT-100, the 5 kW-class P5 and the 600 W-class BHT-HD-600. Similarities and differences in far-field plume properties are identified and discussed. Besides, thruster performances are computed from the beam properties and compared to direct thrust measurements performed with a newly developed micro-thrust scale balance.

Nomenclature

R	= thruster exit plane - probe entrance distance
d	= channel mean diameter
ϑ	= polar rotation angle
φ	= azimuth rotation angle
dS	= elementary surface
I_d	= discharge current
V_d	= discharge voltage
P_d	= discharge power
$\dot{m}_a$	= anode mass flow
$\dot{m}_c$	= cathode mass flow
j_i	= ion current density
$I_{i,tot}$,I_b	= total ion beam current
$\dot{m}_i$	= ion mass flow
V_b	= beam voltage

*PhD. Student, ICARE and Exotrail, thibault.hallouin@cnrs-orleans.
†Research Director, CNRS; Head of EP team, ICARE, stephane.mazouffre@cnrs-orleans.fr.
‡Graduate Student, ICARE.
§Plasma Physics Research Engineer, Exotrail
¶Chief Scientific Officer and Cofounder, Exotrail
‖Chief Technology Officer and Cofounder, Exotrail

E_i	= most probable energy at a given angle
ν_i	= ion mean velocity
ν	= ion mean velocity at a given angle
T	= thrust
Isp_a	= anode specific impulse
η_b	= beam efficiency
η_m	= mass utilization efficiency
η_ν	= voltage efficiency
$\vartheta_{div}, \varphi_{div}$	= ion beam divergence
e	= elementary charge constant, 1.6×10^{-19}C
M	= propellant mass, 2.18×10^{-25}kg for Xenon
g	= gravity acceleration 9.81 m.s^{-2}

I. Introduction

Over the last decade, the satellite miniaturization has opened up a new space market. Technologically simple, inexpensive and flexible, nano- and micro-satellites are well suited for various low Earth orbit missions, communication, science and observation. Propulsion systems have understandably adapted to this new market, through miniaturization and reducing of operating power.

Compare to its chemical counterpart, electric propulsion is appropriated to challenges and needs of the micro-satellites market. In addition to a long operation time, one of the major advantages of electric propulsion is a high attainable exhaust velocity[1]. As a matter of fact, liquid or solid chemical thrusters are limited by the energy per unit of mass stored in the propellant. Thus, the maximum achievable exhaust velocity cannot exceed 5.5 km.s^{-1}. The electric propulsion uses an external energy source to accelerate the propellant. By decoupling energy source and propellant, high exhaust velocity can be reached, only limited by the electrical power delivered by the embedded Power Processing Unit. This creates considerable benefits, such as reducing the propellant fraction resulting in cost reduction and larger payload mass, but also achieving orbit missions requiring high velocity increments[1] (e.g. orbit transfer, satellite displacement, or, in the near future, interplanetary journeys).

Electric propulsion also provides a large panel of technologies with various performances, thereby offering flexibility according to the needs of the mission. In this manner, gridded ion engines will be preferred for interplanetary journey, in view of their high Isp and low thrust performance. By contrast, Hall Thrusters (HT) suit for missions requiring high thrust level, such as drag compensation of LEO satellites and orbit transfer. The latter EP device is a robust and simple technology, producing large Thrust-to-Power ratio and moderate Isp. A HT uses an electrostatic force to accelerate ions. A radial magnetic field is generated by permanent magnets (or coils) inside a dielectric channel and a discharge is established between an inner anode and an external thermo emissive cathode. The crossed electric and magnetic field traps electrons, which locally increases the electron density, hence a high ionization of the gas propellant injected in the discharge channel. The electron mobility is reduced in the region of large magnetic field magnitude, which leads to a well-localized high axial electric field that accelerates the ions. Nonetheless, to answer the needs of micro-satellite markets, HT dimensions have to be reduced to operate the discharge at lower power. This design change brings its share of challenges, namely high power losses to the channel wall and important erosion rate reducing the thruster lifetime. With the aim of optimizing thruster lifespan and efficiency, the understanding of plasma behavior in HT is essential.

Hence, the plume diagnostic represents an interest in terms of understanding the plasma discharge and the thruster near field. Furthermore, ion flows is directly linked to thruster performances, such as the thrust, the specific impulse and the divergence. Henceforth, interrelations can be established between plume properties and HT characteristic dimensions in order to enlarge scaling relations to low power class HTs. Similitudes and differences with high power class HTs could be deducted and, hence, improve numerical simulation outcomes. This deepening understanding provides also key insights to properly dimension diagnostic probes to have the most accurate and reliable measurement by limiting undesired plasma effects.

As well, the knowledge of plume-spacecraft interactions is relevant for spacecraft and electric thruster designers. As a matter of fact, plume particles constantly interact with surrounding areas (namely spacecraft surfaces, solar panels and scientific instruments) and the effects not only on the operation but also on the lifetime of the spacecraft are quite significant. Firstly, momentum of the plume particles impacting the spacecraft may create a torque on the latter, shifting its direction and orientation[2]. Secondly, cumulative processes, such as ion erosion and contamination, can drastically reduce the total lifetime of the satellite, as well as the solar panel performances. These latter mechanisms are mainly due to sputtered and eroded products, stripped off by high-energetic ions of the discharge from ceramic channels and magnetic poles of the HT, and satellite surfaces. The evaluation of the ion beam behavior therefore plays an important role in optimizing both satellite operation and design[2].

In doing so, we measured ion current density and ion energy distribution function by means of a Faraday Cup and a Repulsive Potential Analyzer, respectively, in the far-field plume of the ISCT100 100W-class HT. The probes were set at a fixed distance from the thruster exit plane and scanned a complete front profile of the plume, from $-90°$ to $90°$, $0°$ being the thruster centerline. We investigated several operating points at different discharge voltages and anode mass flow rates. The cathode parameters remained unchanged. We also performed thrust measurements with a home-designed thrust scale balance, developed to measure low thrust in the range of 0.1mN - 10mN. Hence, the present paper presents ion current density and ion energy profiles achieved for each operating point. An analytic study of the thruster performances is achieved and compared to direct thrust measurement. Furthermore, result comparison with diversified power classes HTs are developed and discussed, namely, plume diagnostic of NASA-173Mv2, SPT-100, P5, BHT1500, PPS-Flex BHT-HD-600, BHT-HD-200.

II. Experimental set-up

A. Vacuum chamber

All experiments have been performed in the NExET – stands for New Experiment on Electric Thrusters – vacuum chamber, a stainless-steel cylinder tank 1.8m in length and 0.8 m in diameter. It is fitted with a primary dry pump, that evacuates 400 $m^3.h^{-1}$, and two turbomolecular pumps, with an overall pumping speed of 650 l/s - N_2. A cryogenic panel absorbs heavy-atom gas such as Xenon and Krypton, the two main propellant gases used in electric propulsion. The pumping speed is around 8000 l/s when the 0.5 m^2 cold panel is sustained at 35K. The overall pumping system guarantees a background operating pressure below 5.10^{-5} mBar - N_2, evidently depending on the gas flowrate injected in the electric propulsion device.

B. ISCT100-v2, a 100W-class HT

The ISCT100-v2 (see Figure 1)is a 100W-class Hall Thruster, with performances comparable to the Busek BHT-100. In these studies, the ISCT100-v2 was operated in the geometrical configuration 2S0 – S0 corresponding to the channel cross-sectional area of Russian OKB Fakel SPT-100 thruster – as well, in the magnetic configuration 2B0 – with B0 a standardized magnetic field amplitude[3]. The annular discharge channel is made of BN-SiO_2. A non-magnetic stainless-steel ring anode is placed at the back of the discharge channel, against the internal surface of the outer ceramic wall. The propellant gas is injected homogenously inside the channel through a mullite ring, of which the high porosity allows diffusion of the gas. The magnetic field is generated by means of cylindrical permanent magnet, made of samarium-cobalt (Sm-Co), located in the inner and outer poles. The homogeneous distribution as well as the lens-shape of the magnetic field are provided by a pure iron magnetic circuit, in such a way the maximum magnetic amplitude is reached at the exit plane of the HT, and, the near-zero amplitude in the anode area. In the course of this study, the ISCT100-v2 was connected to a coper plate radiator, used to regulate the thruster body temperature, and, thus, prevent magnets from overheating. The thruster was kept at floating potential, by means of isolating screws.

A 1A-class LaB_6 hollow cathode was used to generate the electron current needed for discharge balance and beam neutralization. The cathode orifice is aligned with the thruster centerline and placed at 5 cm above the thruster inner pole and at 1.5 cm upstream the channel exit plane. The inclination angle is fixed to approximately $45°$. The cathode base plate is floating and electrically connected to the thruster anode, as a reference potential. It should be noticed that the cathode was continuously operated with a heating power, adapted to maintain a constant cathode-to-ground voltage around -8 V.

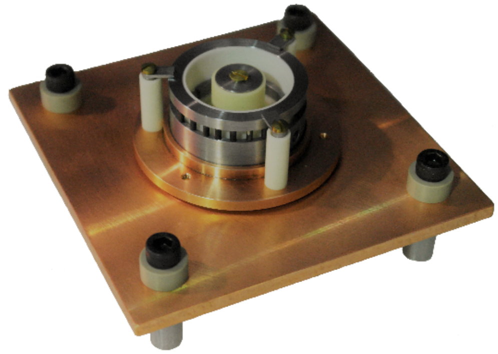

Figure 1: ISCT100-v2, 100 W-class permanent magnets HT

During these experiments, high-purity xenon was used as the propellant gas for both the thruster discharge and the cathode discharge. The cathode has been operated with a constant Xenon mass flow rate of 2 SCCM.

C. Probe design

1. Faraday Cup

A Faraday Cup (FC) is an electrostatic planar probe with an isolated conductive cup (see Figure 2). Compare to conventional planar probes, the FC is appropriated for accurately measuring the ion current density in the far-field plume of HT's. Its specific design makes the measurement insensitive to the edge effects due to plasma sheaths[4,5]. A FC is composed of an entrance aperture, namely the collimator (2), which defines the probe view angle and reduces the amount of ion current. The so-called collimator is encapsulated in a cylindrical cup (4), at the bottom of which is set the collector (5). Insulators are used to decouple the cup from the collimator (3) and to shield the cup from surrounding plasma (1 and 6).

The FC used in the present study is described in referenced papers 4 and 5. The collimator (2) is made of graphite, selected for its low sputtering yield. Its orifice diameter is set to 10 mm, to minimize charge exchange and scattering collisions within the cup. Thus, the surface of current collection is 7.85×10^{-5} m^2. The collimator was set at a floating potential. The collector is made of molybdenum, to limit the secondary electron emission within the stainless-steel cup.

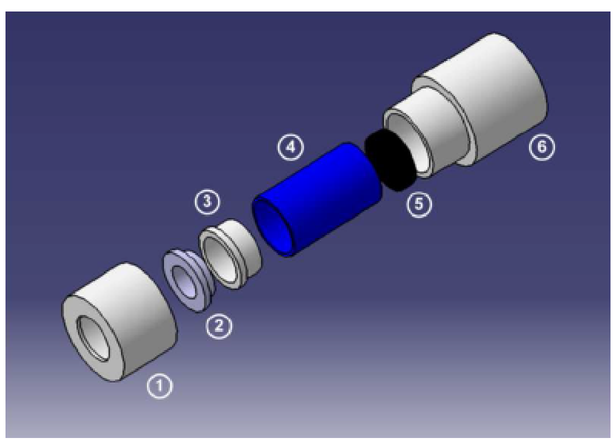

Figure 2: Faraday Cup design

A grounded and calibrated Keithley 2410 1100 V source-meter instrument has been used to measure the collected current. The unit was operated in voltage source to apply a constant negative bias voltage to the probe collector and read value of current. The bias voltage, namely the saturation voltage V_s, was set to -50 V. The influence of V_s is investigated afterward in this paper (see section IV).

2. Retarding Potential Analyzer

A retarding potential analyzer is a plasma diagnostic tool, composed of successive electrostatic grids and a conductive collector. In the present study, a 4-grid RPA[5] has been used. The instrument operates as a filter by determining the ionic current in accordance with the scanning potential. The negative derivative of the I-V characteristic measured provides the Ion Energy Distribution Function (IEDF). Each grid plays an essential role in the measurement[5,6,7], as described below (see Figure 3):

- The first grid (G1) at the aperture of the probe is used as a screen, thus, preventing the other grids from influencing the plasma. The entrance grid is grounded or at a floating potential;
- The second grid (G2) is an electron repeller (ER), biased negatively relative to the plasma potential;
- The third grid (G3) is used as an ion filter. A positive voltage sweep is applied to it, discriminating between ions of different energies. In other words, only ions with an energy higher than the applied potential pass through the filter, the others being repelled and prevented from detection.
- The fourth grid (G4) is a second emissive electron repeller (SER). Ion bombardment within the RPA extracts low-energy electrons. These undesired entities increase the signal noise and distort current measurement. In doing so, the grid is biased negatively to repel electrons.
- The ion collector (C) is a conductive surface biased negatively or grounded. The ions strip electrons off from the conductor which creates a current.

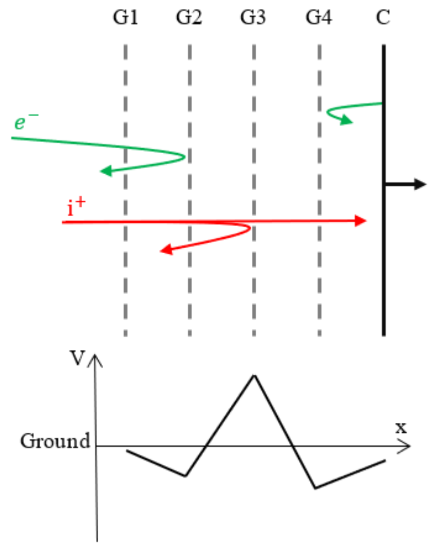

Figure 3: 4-grid RPA scheme

The current RPA design has been developed ensuring a proper electric configuration to guide ions toward the collector. In that way, mesh size is of a few Debye length to adequately discriminate particles of plasma[6]. As for the grid spacing, the gap must prevent from a build up of charge which would negate the effect of the previous biased grid. Thus, the standard space is approximately four times the Debye length[8]. A collimator is placed upstream the screen grid, in the same purpose as the one of the FC, that is regulate the ion flux and define the probe view angle. Furthermore, material selection is essential to guarantee accurate measurement. PEEK grid mounts are used to avoid short circuits induced by material sputtering and conducting-coating formation. The collector is made of Molybdenum, a low secondary electron emission (SEE) yield material, and grids in stainless steel. Characteristic dimensions of the 4-grids RPA operated during these experiments are presented in Table 1.
As part of this study, the shielding grid G1 was floating, G2 was negatively biased at -15 V, G3 voltage was swept between 0 V and 400 V, G4 fixed at -20 V, and the collector slightly biased negatively at -5V. G2, G3 and the collector voltages were monitored by the Semion control unit from Impedans Ltd and I-V characteristics were recorded and plotted on the software interface.

It is worth noting that a RPA is unable to differentiate singly charged ions and multiply charged ions. Indeed, the current measured is dependent on the energy per unit charge of ions. For instance, a singly charged particle I^+ with 300 eV of energy and doubly charged particle I^{2+} with 300 eV of energy are identically probed by the RPA.

The probes (FC and RPA) were mounted on an aluminum rotating arm, thin enough to limit plasma inter-

Table 1: RPA - Characteristic dimensions

RPA - Characteristic dimensions[5]	
Mesh size [mm]	0.4
Collection area [mm^2]	78.5
Diameter [mm]	45
Length[mm]	40
Transparency [%]	60.2
Distance between grids [mm]	2
Collimator diameter [mm]	10

action in the vicinity of the measuring tools. The pivot point coincides with the exit plane of the thruster and is aligned with the thruster centerline as described in Figure 4. The probe centerline is cofounded with the revolution axis of the thruster. The distance between the entrance aperture of the probes and the exit plane of the thruster was set at a distance of 31.5 cm, nearly 10 times the discharge channel diameter of the HT. The rotation motion is achieved by means of the Newport URS100BCC motorized rotary stage. The rotation angle ϑ is varied between $-90°$ and $90°$ with a step of $5°$, satisfying the condition[9]: $Rd\theta \geq d$. The thruster centerline corresponds to $\vartheta = 0°$.

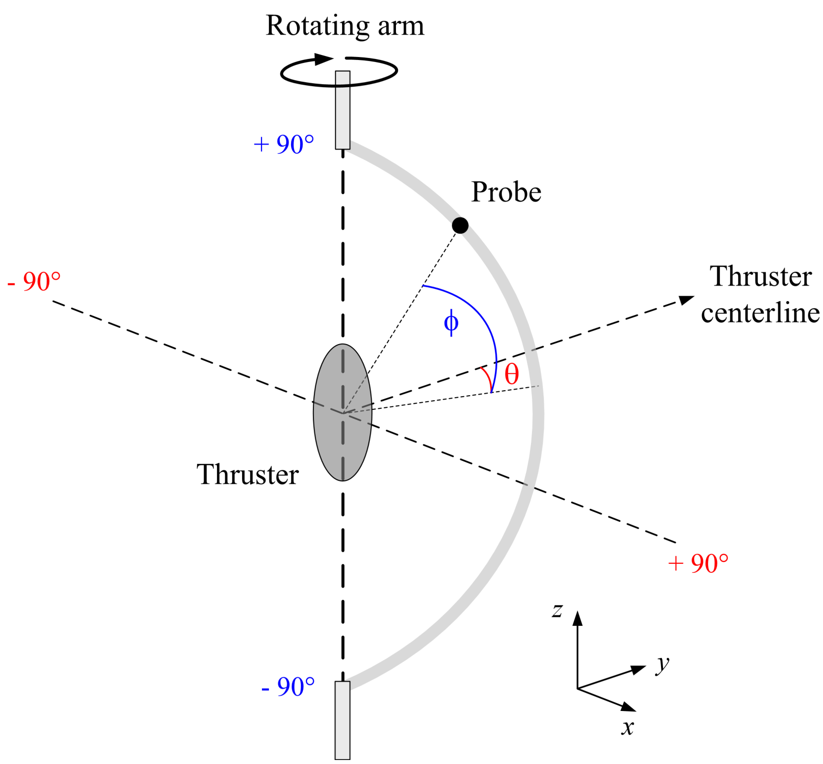

Figure 4: Experimental set-up illustration

D. Thrust scale balance design

In parallel, thrust measurements were performed by means of a thrust scale balance (see Figure 5). Designed and developed within the ICARE laboratory, this balance meets the needs of low-power electric propulsion systems, namely the measurement thrust range of 0.1mN to 10mN. A balance presents the advantage of being a non-immersive performance tool, measuring the displacement induced by a thrust and thus assess the latter. The system must nevertheless deal with numerous error sources, impacting the accuracy and the repeatability of the measurements. Inaccuracy is mainly generated not only by interference noise – close to the thrust magnitude – induced by the pumping system and the laboratory environment, but also, by the framework and sensor thermal drift imposed by the thruster operation. The choice of the present design has been thoroughly investigated and will constitute a later publication. As the balance is a first draft, the overall framework is made of aluminum, selected for its cost-effectiveness. The next version will be manufactured in titanium, to limit thermal expansion and conductivity within the structure. Noticeable parts are succinctly described in the following subsection.

The current balance is a simple pendulum composed of a movable arm attached to two Riverhawk flexural

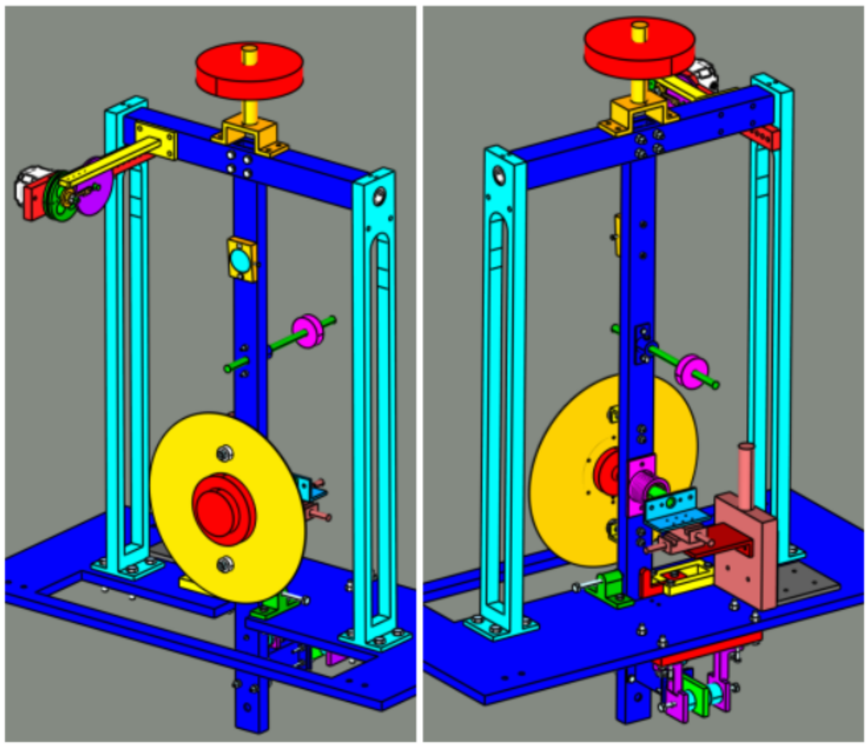

Figure 5: Complete CAD model of the thrust balance

pivots. At the top of the mobile part, a counterweight is used to increase the maximum displacement at the sensor position. Moreover, an adjustable balancing system counterbalances the moment produced by the weight of the thruster. Otherwise, a magnetic damping system is placed at the bottom of the pendulum to limit parasitic oscillations. It is composed of two fixed cylindrical permanent magnets between which a copper plate is moving in accordance with the moving arm. An eddy current brake is then induced in the copper piece by the motion of the magnetic field through the conductor. Furthermore, calibration is required before and after each thrust measurement to consider the thermal drift in the thrust measurement. It operates through the application of a well-known force to the pendulum generating a displacement. The relation force-displacement can be graphically plotted and used to determine the actual force generated by the thruster. The integrated calibration systems have been designed in such a way the calibration forces contain the required thrust range measurable. Hence, two systems have been conceived, viz pre-calibrated weights and voice coils. The first system relies on the measurement of the displacement incurred by the gravitational force of four lead pre-calibrated weights. A stepper motor attached to a pulley changes the number of applied weights and thus the displacement. The second mechanism generates a force by passing a known electrical current through a coil, that repels a magnetic circuit, fixed on the moving arm of the device. For each applied current matches a known force, and thus, a displacement. Finally, displacement measurements are provided by both an inductive sensor and a custom triangulation-based optical sensor. In this study, only the second system was operated as a result of its higher resolution and accuracy, its insensitivity to temperature variation and vacuum environment.

The ISCT100-V2 HT is attached to a circular aluminum radiator and is at a floating potential, relative to the grounded balance. The 1-A external cathode is located on the stationary part of the balance and electrically isolated from the structure.

III. Computed quantities

A. Total ion current and divergence

In the analytical study, the plasma is assumed to originate from a source point, since $R \approx 10d$. The total ion current in the beam $I_{i,tot}$ is equal to the integral of the ion current density j_i over an elementary surface at a fixed distance R[9,10].

$$I_{i,tot} = \int_{-\pi/2}^{\pi/2} \int_{-\pi/2}^{\pi/2} j_i(\vartheta, \varphi) dS \tag{1}$$

In spherical coordinates, the elementary surface is defined by polar and azimuth angles, ϑ and φ respectively, as: $dS = R^2 sin(\vartheta) d\vartheta d\varphi$. The quantity $j_i(\vartheta, \varphi)$ is not experimentally measured directly. Instead, only $j_i(\vartheta, 0)$ is probed. We assume the plume properties are isentropic with respect to the thruster axis, that is $j_i(\vartheta) = j_i(\varphi)$. We obtain the new equation:

$$I_{i,tot} = \pi R^2 \int_{-\pi/2}^{\pi/2} j_i(\vartheta) sin(\vartheta) d\vartheta \tag{2}$$

The beam divergence is defined as a domain which contains 90% of the ion beam current. Its boundaries are set by the ion beam divergence half-angles, namely ϑ_{div} and φ_{div}. As a consequence of the isentropic-plume assumption, both angles are equal. The divergence half angle is deduced from:

$$0.9 I_b = 2 \times \pi R^2 \int_0^{\vartheta_d iv} j_i(\vartheta) sin(\vartheta) d\vartheta \tag{3}$$

B. Thrust and specific impulse

A simple expression of the thrust is[2]:

$$T = \dot{m}_i \times \nu_i, \tag{4}$$

Where ν_i is the ion mean velocity in the beam and $\dot{m}_i$ the ion mass flow rates. The latter is given by[2]:

$$\dot{m}_i = \frac{M}{e} I_{i,tot}, \tag{5}$$

where e and M are the elementary charge and the propellant atom mass, repectively.

We assume that the plume is only composed of singly charged ions. Thus, by considering the ion energy and current density distribution along the angular profile, we obtain:

$$T = \frac{M}{e} \pi R^2 \int_{-\pi/2}^{\pi/2} j_i(\vartheta) sin(\vartheta) \nu(\vartheta) cos(\vartheta) d\vartheta, \tag{6}$$

with $\nu(\vartheta)$ the mean ion velocity at a given angle determined from the ion kinetic energy and $\cos(\vartheta)$ accounting for symmetry in radial momentum.
The anode specific impulse is given by the following equation:

$$Isp_a = \frac{T}{\dot{m}_a g} \tag{7}$$

C. Efficiencies

Within an HT, thruster performances and plasma properties are closely related. Thereupon, some quantities can be determined to report on the ISCT100 efficiency. Therefore, following quantities are determined thanks to ion beam properties, namely ion current and ion mean energy[2]:

– The current efficiency describes the fraction of discharge current used to produce ion beam,

$$\eta_b = \frac{I_b}{I_d}, \tag{8}$$

– The mass utilization efficiency corresponds to the ionization efficiency of the propellant gas

$$\eta_m = \frac{\dot{m}_i}{\dot{m}_a}, \tag{9}$$

– The voltage efficiency compares the applied discharge voltage to the beam voltage

$$\eta_\nu = \frac{V_b}{V_d} \tag{10}$$

IV. Experimental results and discussion

A. Ion current density profiles and beam current

1. Influence of the FC bias voltage

As a first step, the angular profile of the ion current density J_i was measured at three different FC bias voltages, namely -25 V, -50 V and -75 V as displayed in Figure 6. The thruster discharge voltage was set to 200 V, with 5 SCCM of Xenon flowing through the anode. The total ion current is computed and presented in Table 2. As expected, the three angular distributions are similar, such as the ion beam currents. These similarities in measurement reveal that the FC is insensitive to the existence of plasma sheath expansions given its specific cylindrical design. In the course of this study, the FC was biased at -50 V, far enough from the plasma potential to limit influence of electrons on the measurement[4].

Table 2: FC measurements - Influence of the biased voltage

U_d [V]	$\dot{m}_a$ [SCCM]	I_d [A]	V_s [V]	$I_{i,tot}$ [A]
200	5	0.38	-25	0.2768
200	5	0.38	-50	0.2773
200	5	0.38	-75	0.2797

2. Repeatability of J_i measurements

The repeatability over time of the measurement is also investigated for a fixed operating point: 200 V, 5 SCCM. The FC measurements were recorded not only at five-hour interval but also at two consecutive times. The angular profiles of J_i are shown in Figure 7 and the respective ion beam current in Table 3. A discrepancy in the maximum amplitude of the J_i distribution is noticeable in the range of $[-20°; 20°]$. One possible explanation for this gap could be due to sputtering materials and deposition on both the probe and thruster body. The FC is an intrusive plasma probe and its long duration exposure to the beam ions can generate sputtering and deposition of materials on the probe collection area, modifying collector surface properties and electrical characteristics of the probe[11]. This reason might be consistent, since the discrepancy is more relevant for the five-hour interval measurements, in other words, after several hours of probe exposure in the thruster plume. Another possible reason would concern the thermal change of the thruster over the study period, affecting the discharge properties. Nevertheless, the total ion current remains constant in time. $I_{i,tot}$ is not or weakly impacted (maximum deviation $\sim 3\%$) by time variation of plume properties.

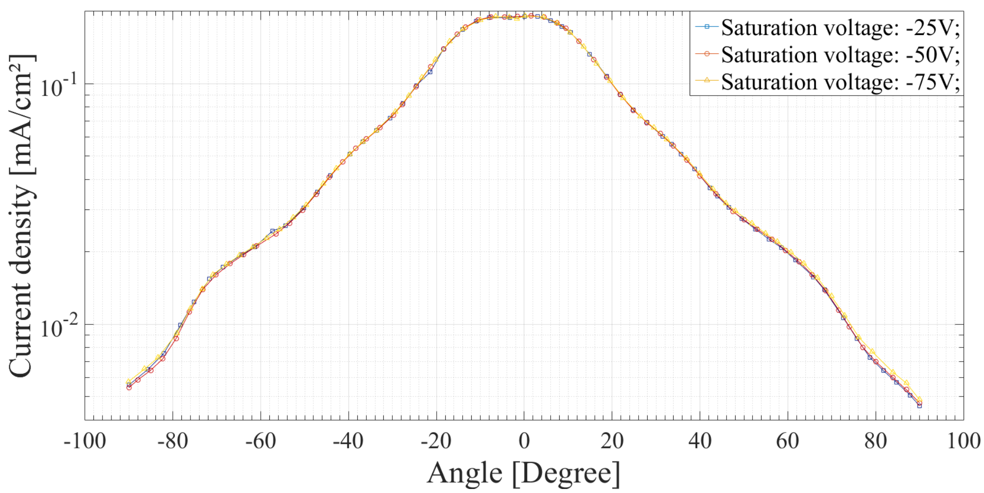

Figure 6: Ion current density profile for different bias voltage (-25 V, -50 V, -75 V)

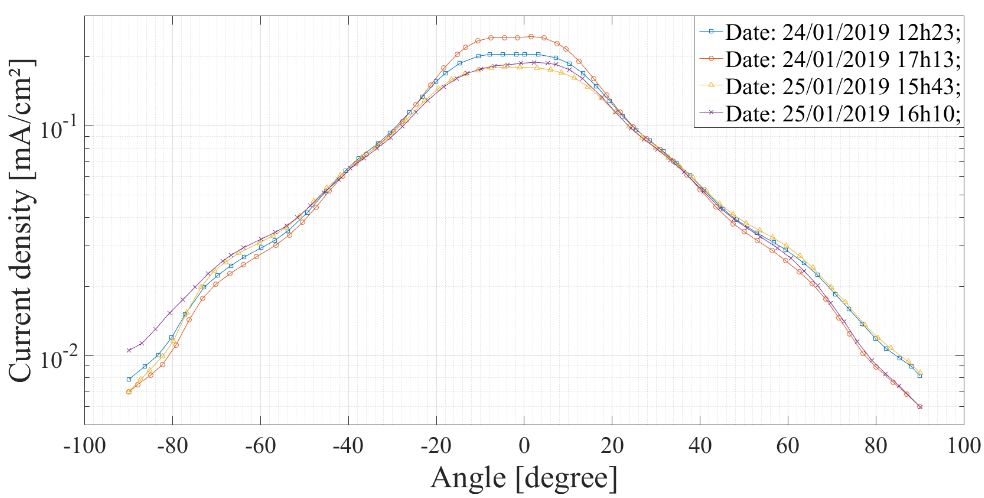

Figure 7: Ion current density profile - repeatbility in time

Table 3: FC measurements - repeatability

Date [d-m-y h:min]	U_d [V]	$\dot{m}_a$ [SCCM]	I_d [A]	V_s [V]	$I_{i,tot}$ [A]
24-01-2019 12:23	200	5	0.36	-50	0.2805
24-01-2019 17:13	200	5	0.38	-50	0.2773
25-01-2019 15:43	200	5	0.36	-50	0.2749
25-01-2019 16:10	200	5	0.36	-50	0.2715

3. Influence of the thruster operating parameters

The overall shape of the J_i angular profile remains similar in many features whatever the operating conditions, as shown in Figure 7. Indeed, the distribution is axisymmetric with respect to the thruster centerline ($\vartheta = 0°$) and reaches a maximum amplitude at this point. By moving away from the thruster centerline, the ion current density sharply decreases by an order of magnitude. Around ±60°, a slightly rising is observed. This wing structure has already been noticed and identified as a backpressure effect[12], as describe in the following section. The shape of J_i profile is similar to the ones observed for high-power HT plumes[17,24,25].

INFLUENCE OF $\dot{m}_a$

Figures 12a and 12b (see appendices) show the J_i angular distribution at fixed discharge voltages (200 V and 300 V) and different anode mass flows. As expected, the total ion current increases with the anode mass flow as presented in the Table 4. Also, as the neutral density increases in the discharge channel of the HT, the ionization event becomes more likely, favoring production of ions. Nevertheless, interesting features are noticeable in the J_i distribution. Firstly, the broadening of the ion current distribution extends since the mass flow rate increases. Secondly, the ion current density in plume-core complies with a limit value, at both 6 SCCM and 7 SCCM, whatever the discharge voltage.

The first feature is commonly observed in FC measurements and is identified as a consequence of backpressure. M.L.R. Walker and Al[12] have investigated the effect of this parameter on the ion current density measurements in the P5 HT plume. The latter was operated at two different backpressures 1.7×10^{-5} mBar-Xe and 4.7×10^{-6} mBar-Xe for a nominal operating condition (300 V, 4.3 A). The difference between the two measurements was estimated at around 7% at the thruster centerline and continuously expands at large angles (90% at 90°). The large difference observed along the plume perimeter is well understood and has been identified as the product of CEX collisions between residual neutral atoms and fast ions. Indeed, if we consider a CEX collision occuring between a fast moving Xenon ion Xe^{+}_{fast} and a slow moving neutral Xe^{0}_{slow}, we obtain the product Xe^{0}_{fast} and Xe^{+}_{slow}. The Xe^{+}_{slow} is pushed to large angles, since its energy is not sufficient enough to overcome plume potential hump at the thruster centerline. Thus, as the backpressure increases with the mass flow, CEX events are more likely and result in an increasing of the current density at the wings.
The ion current density was also measured with a planar probe in the plume of the PPS-Flex[9]. Measurements were performed at various pressure levels to identify backpressure effects. The PPS-Flex was operated with a standard magnetic configuration at 250V with 3.5 mg/s of Xenon injected in the anode chamber. Figure 8 dinstinctly confirms previous observations, namely the core of the plume is unaffected by pressure effects in contrast to large angles, where the current density is increased by 525%[9]. Note that for 5×10^{-5} mBar the profile is distorted: the thruster is not operating in a standard mode due to backpressure effects. Thereupon, the backpressure condition is determinant in the reliability of ion current measurement as shown in figure 9. As the backpressure increases, the total ion current is overestimated, resulting in an increase of thruster performances[9]. Furthermore, it can be noticed that the ion current is much larger than the discharge current (see Figure 9). This phenomena is a direct consequence of the probe design used, as the planar probe is sensitive to plasma sheath expansion[4,5]. As a consequence, the collection area increases, resulting in a rise of the current collected.
The second feature discussed above can also be the consequence of backpressure effects. Since the CEX ions are redirected to large angles, the ion current density in the core of the plume is decreased. Nevertheless, other tendencies were described in litterature[25] and lead us to consider other explanation, related to the inherent properties of low-power HT.

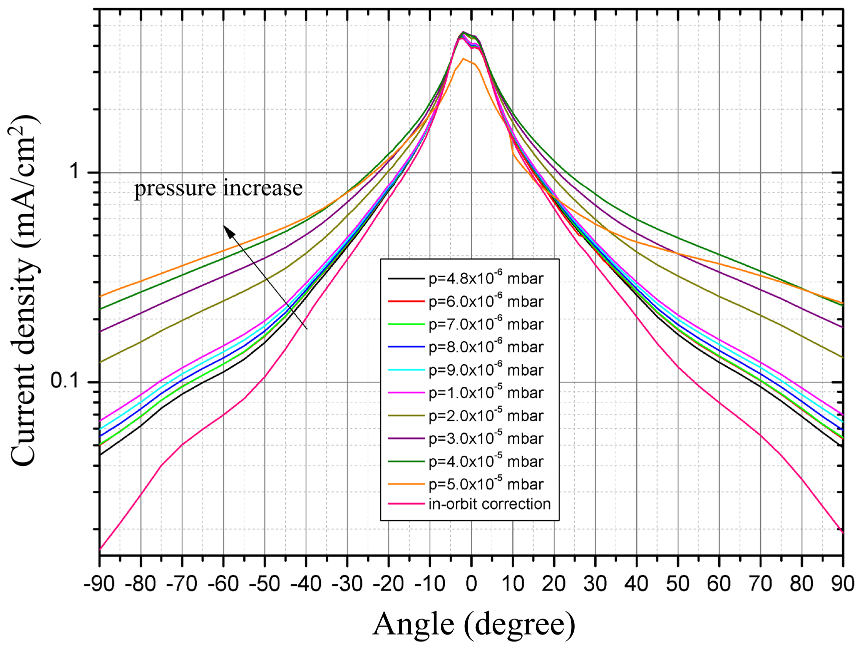

Figure 8: PPS-Flex - Current density profile[9]

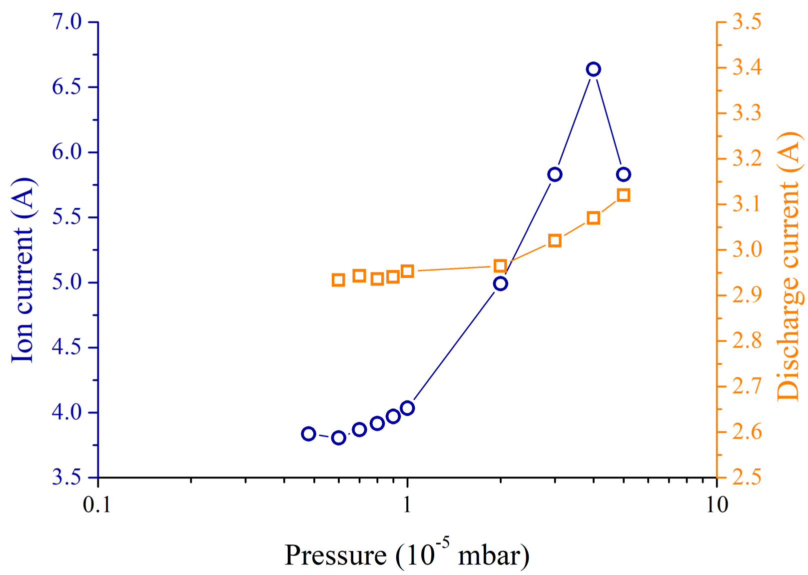

Figure 9: PPS-Flex - Total ion current and mean discharge current.

Influence of U_d

The influence of the thruster discharge voltage is investigated for three different anode mass flows, that are 5 SCCM, 6 SCCM and 7 SCCM. The J_i angular profiles of respective mass flows are plotted in Figures 13a,13b,13c. Common features are identifiable. Firstly, for angles wider than $\pm 40°$, the ion current density increases when the discharge voltage is ramped up. Secondly, the current density remains constant in the range of $[-40°; 40°]$, at a given mass flow and whatever the discharge voltage (especially for 6 SCCM and 7

SCCM).

The first observed feature diverges from common observations as it is the case for the BHT-HD-600[17]. Jared M. Ekholm and Al. figured out that an increase in discharge voltage leads to a narrowing of the profile and a growth of the central peak. As a comparison, the Full-Width at Half-Maximum (FWHM) was computed in the course of this study and plotted as function of the discharge voltage (Figure10). The FWHM parameter accounts for the profile dispersion. The plot clearly shows the discrepancy in terms of the narrowing evolution between the two thrusters. Except at the 5 SCCM operating point, the ISCT100-v2 profile dispersion increases with the discharge voltage, in contrast to the BHT-HD-600.

The discrepency can not be attributed to backpressure effects, since the gas injected through the anode

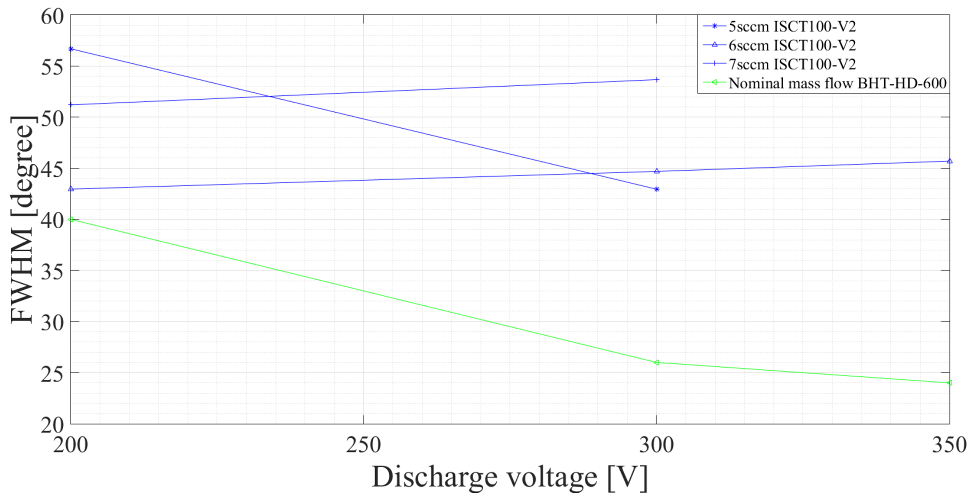

Figure 10: FWHM for ISCT100-v2 and BHT-HD-600 J_i profiles

remains constant and thus, the residual pressure in the vacuum chamber unchanged. In this instance, the rise of the wing-shape distribution can be the result of several phenomena, occurring with the ramp-up of the discharge voltage. Firstly, as mentioned in several articles [13,14,15], high discharge voltage operation favors multiply charged ions production, of which the population increases at large angles. Secondly, the electric field distribution is also impacted by an increase of voltage, in such a way the fraction of potential inside the thruster increases, shifting the location of the ionization area downstream and extending the acceleration region[16]. Finally, the geometric divergence of the thruster plume increases with U_d, forming radial components in the electric field. Slow moving ions resulting of CEX collisions are more susceptible to local electrostatic forces: they are accelerated radially, to large angles.

The second observed feature was already mentionned by D. H. Manzella and J. M. Sankovice in the SPT-100 plume[24], although main of investigations do not report this trends but rather an increase of J_i on the thruster centerline[17,25]. The asymptotic limit is presumably a consequence of multiply charged ion production. The electron temperature increases with the discharge voltage[10], resulting in increasing the fraction of multiply-charged ions. These entities are accelerated to large angles.

B. Ion energy distribution function

1. *Repeatability of RPA measurements*

The repeatability over time was also investigated in the course of the ion energy distribution function (IEDF) measurements. The two measurements were recorded at two-hour interval, with the thruster firing at 200 V with 5 SCCM of Xenon flowing through the anode. Figure 11 shows the most probable energy (a), i.e. the primary energy peak, and the mean energy (b). It appears that the most probable energy remains constant over time, unlike mean energy, of which discrepancies are observed (~12 V at small angles and ~6 V at large angles). This gap may be the consequence of the fluctuation of CEX and elastic collision events, as far as the background pressure slightly increases in time (3.5x10^{-5} mBar-N_2 to 4x10^{-5} mBar-N_2), due

Table 4: Ion beam current for each investigated operating point

U_d [V]	$\dot{m}_a$ [SCCM]	I_d [A]	P_d [W]	$I_{i,tot}$ [A]
200	5	0.36	72	0.2805
300	5	0.44	132	0.3191
200	6	0.46	92	0.3499
300	6	0.53	159	0.3901
350	6	0.58	203	0.4097
200	7	0.55	110	0.4293
300	7	0.67	201	0.4769

to the less effectiveness of the cryogenic pump. An other likely explanation would concern the change of plasma properties owing to variation in both the magnetic and electric fields shapes, affected by the thruster warm-up[18].

2. Low-energy ion flux

Thanks to I-V characteristics measured with the RPA, we can deduce the ion distribution as a function of the angle and energy levels (see Figures 14a and 14b). For instance, the RPA 0 curve corresponds to ion quantity of which the energy is higher than 0 eV (i.e. the ion current probed by the FC). Likewise, the RPA 10 corresponds to ion quantity of which the energy is higher than 10 eV. The difference between the two curves provides a good assessment of 10 eV-ion distribution along the angular profile. Here, the concern is to represent distribution function of low energy ions (<100 eV), at a nominal flow rate (5 SCCM) and two discharge voltages (200 V and 300 V). The two profiles remain similar, as the amount of low-energy ions increases moving off the thruster centerline. In the vicinity of 0°, curves are tightened, indicating the absence of low energy ions in the core of the plume. At this point, we can identify a main difference between the two profiles. For $U_d = 200V$, slow-ion population appears hereafter 20° against 30° for $U_d = 300V$.
Similar measurements has been perfomed by Diamant and Al.[21,22] with both PPS®1350-G and SPT-100 HTs. By comparison with the ISCT100-v2 analysis, we observe that the distribution is identical for the core of the plume but remains different at larger angles. Indeed, in Diamant's papers, a large gap appears between RPA 0 and RPA 20 curves, as the angle increases. This large difference is not observable anymore with energy higher than 20 eV. In other terms, slow ions population of which the energy is lower than 20 eV are only present at large angles. In the case of the ISCT100-v2 diagnostic, we clearly see that the ion population distribution is more disparate at large angles, with the presence of intermediate energy ions, as discussed in the following section.

3. Far-field ion energy at low and high discharge voltages

The ion energy distribution function is investigated at low and high discharge voltages (200 V and 300 V, respectively) with 5 SCCM of Xenon injected. The two series of curves are shown in Figures 15 and 16.

For the low discharge voltage case, at the centerline of the thruster ($\theta = 0°$), a primary peak is visible at 186eV, 93% of the discharge voltage. The difference between these two values is in part the consequence of the Cathode Return Potential (CRP), that is the energy required to extract electrons from the 1A-cathode. As previously mentioned, the CRP was maintained to -8 V in the course of this study, by adjusting the heating power. The last missing portion is used to ionization and converted into radial motion[16]. Furthermore, a small population of lower energy ions is existent around 120eV, that is $2/3V_i$. At 20° and 40°, the primary peak energy values drop a couple of volts, 181eV and 175eV respectively. These two primary-ion populations are probably created further downstream in the ionization region, facing a lower potential than the ions found at 0°. Moreover, a large population of intermediate energy ions are visible, and the amount increases with angle. From 60°, low-energy ions (57eV) dominate the energy distribution. At this point, the primary population is still existing, but at a smaller amount. Ion-ion collisions are also recognizable and become predominant as compared to smaller angles. Lastly, at 80°, the primary ion population sharply decreases. The energy distribution is only dominated by low-energy ions.

For the high voltage case, similar features are observable at angles strictly slighter than 60°. Indeed, the

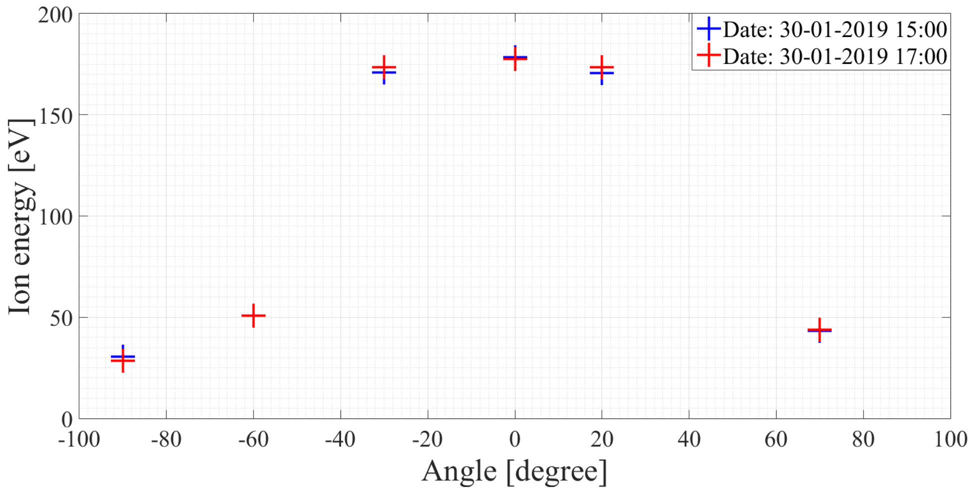

(a)

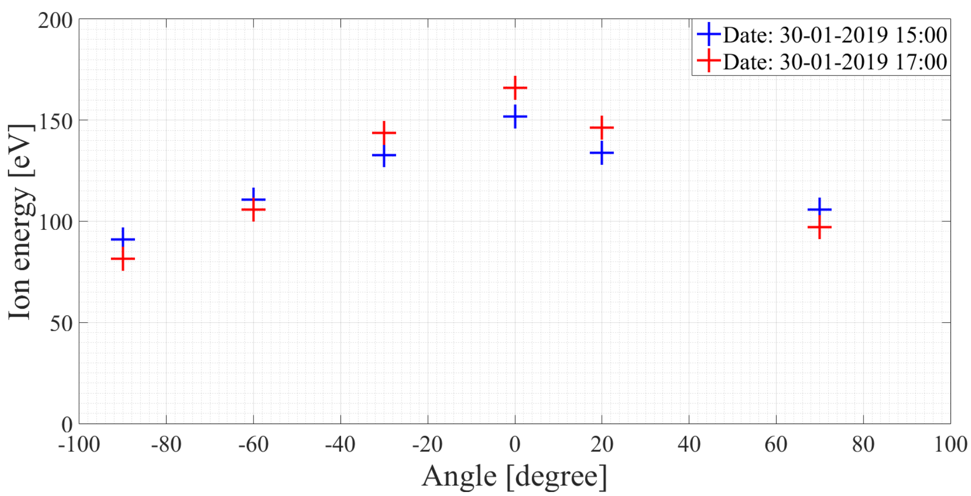

(b)

Figure 11: Repeatability of RPA measurements (a) most probable energy, (b) mean energy

centerline of the thruster is dominated by a high-energy peak of 286eV, 95% of the applied discharge voltage. Nevertheless, at 60°, a significant difference is noticed compared with the low voltage condition. At this point, the high-energy peak is still predominant compared to other energies. A large amount of low-energy ions also appears around 65 eV ($\sim 1/4 V_i$). At 80°, the dominant peak finally shifts toward low energies. Ion-ion CEX/elastic collisions products are still observable at each angle. This discripency
Similar ion populations were pointed out in the BHT-1500 plume[26]. The aformentionned intermediate energy ion population has been identified as the result of two mechanisms. Firstly, source ions undergo elastic collision resulting in the loss of momentum: the probed ion is less energetic. Secondly, as mentionned previously, some ions are created downstream from the ionization region, consequently facing a potential lower than the discharge voltage. CEX collisions between singly and multiply charged ions can also play a role in the creation of this ion population but at a lower level.

4. Mean energy and most probable energy

The most probable energy represents the dominant peak of the ion energy distribution, that is the maximum of the IEDF. At a given angle, the mean energy is obtained with the following equation:

$$E_{mean} = \frac{\int_0^{V_{max}} \frac{\partial I}{\partial V} \times V dV}{\int_0^{V_{max}} \frac{\partial I}{\partial V} dV} \tag{11}$$

With V_{max} the upper limit value of the filtering bias voltage.

The evolution of both the most probable (E_{max}) and mean energy (E_{mean}) are plotted as function of the angle, for each operating point (see Figure 17). Regarding the E_{max} distribution along the angular profile, the drop at ±60° and ±80° is clearly identified, for low and high discharge voltages respectively. It confirms the trend observed in the previous section. Furthermore, below this drop, the E_{max} distribution is maximum around 0° and remains quite constant towards larger angles. This trend confirms previous findings, namely that this section of the plume is dominated by high-energy ions. Hereafter the drop, E_{max} decreases continuously (in average 1eV/degree). Nevertheless, the E_{mean} distribution shape remains similar whatever the discharge voltage and common features can be pointed out. Firstly, the mean energy is maximum at the thruster centerline, since the ion beam is dominated by source ions and less disturbed by collision events. Secondly, the distribution follows a winged shape, clearly visible at ±30° and ±70°. Thirdly, between each identified levels, the mean energy distribution steadily decreases, as the low-energy ion population increases with angles. Similar tendencies were observed in the plume of the BHT-600 Hall Thruster[27].

Figure 18 offers a new illustration of IEDF within the thruster plume, for two operating points: 200 V, 5 SCCM and 300 V, 5 SCCM. These two plots distinctly show that most of the beam energy is concentrated within $[-20°; 20°]$, whatever the discharge power. At these two limits, two trails extend towards low energies, expressing the emergence of slow ions at high angles. Fast ions gradually fade as the angle increases, until fully vanishing at ±60° and ±80°. Furthermore, significant ion population of which the energy is greater than the discharge voltage is observable in the far-field plume, especially at high voltage. This supra-sped ions population was already observed in previous publications [16,19]. The mechanisms spearheading the supra-sped ion production in the far field plume of a HT might be the charge-exchange collisions and momentum transfer processes between singly and multiply charged ions. Thus, very fast ions are continuously produced along the ion beam and visible only in the thruster far-field plume, as the mechanism is efficient for long mean free paths. Since the multiply charged ion amount increases with the discharge voltage, the mechanism is in accordance with previous observation.

C. Thruster performances

The thruster perfomances can be deducted from RPA and FC measurements as described in the section III. Table 6 gathers perfomance parameters obtained for achieved operating points. As shown, the beam efficiency (i.e. current utilization) is above 0.7 and decreases with respect to discharge voltages, as a result of an increasing of mulitply-charged ions population. The mass utilization efficiency is above 0.8 and increases with the discharge voltage. This value reveals a good ionization efficiency of the ISCT100-v2. The voltage utilization is around 0.7 and increases with discharge voltage. The divergence half-angles remains around

80°, and decreases as the discharge voltage is ramped up[25,26]. Compared to other power-class HT, some efficiencies are similar. Indeed, the 5kW-class NASA-173Mv2[2,27] and the 600W-class BHT-600 HTs[28] have similarities efficiencies as presented in Table 5. Beam and mass utilization efficiency are identical. Only the voltage utilization efficiency remains different, as the ratio increases with the power discharge. This discripency might be explained by the fact that the operating range of high power class HT is more flexible, enabling to apply high discharge voltage.

Table 5: HT performance comparison

HT	**Power**	η_b	η_m	η_ν
BHT-600	600 W	0.79	0.94	0.77
NASA-173Mv2	5 kW	0.77-0.81	0.86-0.9	0.89-0.97

Thrust measurements are summarized in Table 7. The agreement between both direct and indirect measurements is correct within 20%. Evolution tendencies of thrust remains similar as the one previously described, as the thrust increases with both the discharge voltage and anode mass flow. It should also be noticed that the indirect measurement always give larger thrust values. The main reason of this trend can be explained by the fact that multiply charged ions are not considered. By integrating these entities in the thrust computation, the resultant thrust might be lower, since multiply-charged ions degrade thruster perfomances[2,29]. Indeed, multiply-charged ions require more energy per unit of charge to be produced and an equivalent acceleration voltage generates $\sqrt{n}$ of the thrust, n being the ion charge. Other sources of error[9] can also be identified as the measuring instrument, the in-time thruster behavior and the data analysis and treatment.

Table 6: Thruster performances

Operating parameters				**FC**	**RPA**	**Thruster performances**					
U_d [V]	$\dot{m}_a$ [SCCM]	I_d [A]	P_d [W]	$I_{i,tot}$ [A]	E_{mean}[eV]	η_b	η_m	η_ν	T [mN]	Isp_a [s]	ϑ_{div} [°]
200	5	0.36	72	0.2805	126.2	0.779	0.764	0.631	4.12	824	80.4
300	5	0.44	132	0.3191	180.9	0.725	0.87	0.603	5.72	1144	77.7
200	6	0.46	92	0.3499	125.6	0.761	0.795	0.628	5.41	902	84.8
300	6	0.53	159	0.3901	219.4	0.736	0.886	0.731	7.07	1178	77.5
350	6	0.58	203	0.4097	269.0	0.706	0.93	0.769	8	1333	78.7
200	7	0.55	110	0.4293	124.1	0.781	0.836	0.620	6.41	916	84.2
300	7	0.67	201	0.4769	232.1	0.712	0.928	0.774	8.73	1247	77.2

Table 7: Thrust measurements

Operating parameters		**Thrust scale**		**RPA/FC**		**Relative error**
U_d [V]	$\dot{m}_a$ [SCCM]	I_d [A]	T [mN]	I_d [A]	T [mN]	δ_r [%]
200	5	0.34	3.8	0.36	4.12	7.8
300	5	0.42	4.8	0.44	5.72	16.1
200	6	0.45	4.6	0.46	5.41	15
300	6	0.56	6.5	0.53	7.07	8
350	6	0.55	7.3	0.58	8	8.75
200	7	0.54	5.7	0.55	6.41	11.1
300	7	0.65	7.9	0.67	8.73	9.5

V. Conclusion

In the course of this study, we have measured ion current density and ion energy in the far-field plume of the 100W-class ISCT100-v2 HT, by means of a Faraday Cup and a 4-grid RPA, respectively. The impact of both anode mass flow and discharge voltage was investigated and compared with far-field plume diagnostics of high power HT's. It appears that the current density profiles remain similar for any class HT, even though 100W-class HT is more sensitive to operating parameters. Indeed, in the core of the plume, the ion current density reaches an upper limit from a certain mass flow. The real cause still remains misundertood (inherent properties of the 100W HT, background pressure effects) and calls for deepening experimental experiments. As well, the ion energy distribution function has also revealed some interesting features. The ion energy is mainly concentrated in the core of the beam $[-20°; 20°]$ and the low energy ion population increases to large angles, result of charge exchange and elastic collisions between different entities. Moreover, the primary peak shifts to lower energy at $\pm 60°$ and $\pm 80°$ for low and high discharge voltage cases, respectively.

Finally, based on those results, thruster performances (namely the thrust, the specific impulse, the divergence and the efficiencies) were also computed and compared to high power HT's. In the same time, thrust measurements were perfomed in parallel by means of a new design micro-balance. Result comparison were discussed as a first assessment of the measurement accurancy.

Given the relevant impacts of backpressure, it appears necessary to improve the operating pressure within the vacuum chamber. Furthermore, it is required to investigate multiply-charged ion population in the far-field plume of a 100W-class HT to refine the overall analysis. As far as we know, ExB probe measurement have never been performed in the course of 100W-class HTs.

VI. Acknowledgement

The authors thank M. Inchingolo for the design, development and commissioning of the thrust balance and T. Gerard for his involvement in the experimental campaign. T. Hallouin benefits from an Exotrail Ph.D. grant. This study was performed within the framework of the ORACLE joint-laboratory program. It has been partly supported by the Region Centre-Val de Loire council in the frame of the PEPSO-2 project.

Appendices

Figure 12: Influence of $\dot{m}_a$ at nominal discharge voltages (a) 200 V, (b) 300 V

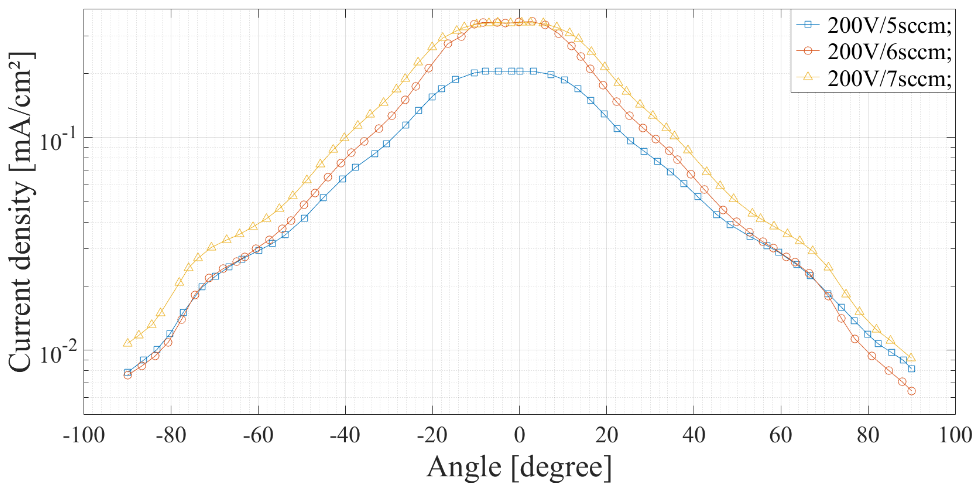

(a)

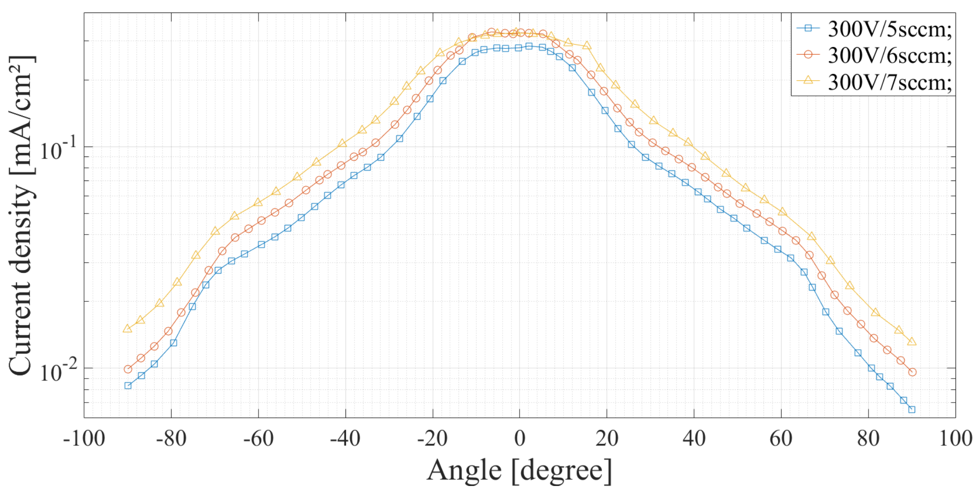

(b)

Figure 13: Influence of U_d at nominal anode mass flows (a) 5 SCCM, (b) 6 SCCM, (c) 7 SCCM

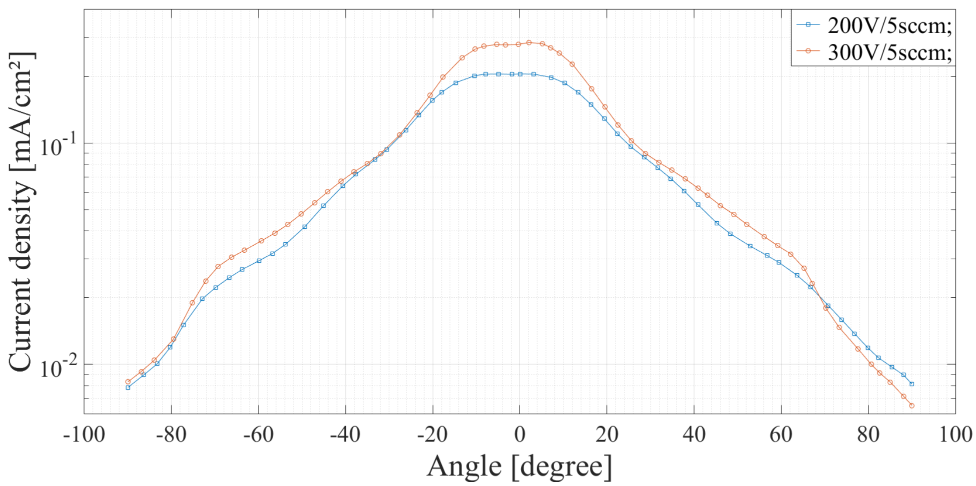

(a)

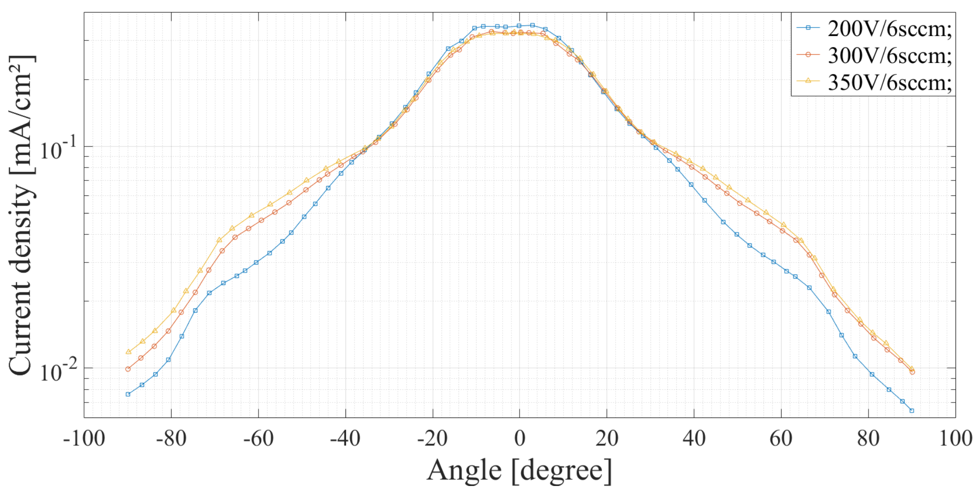

(b)

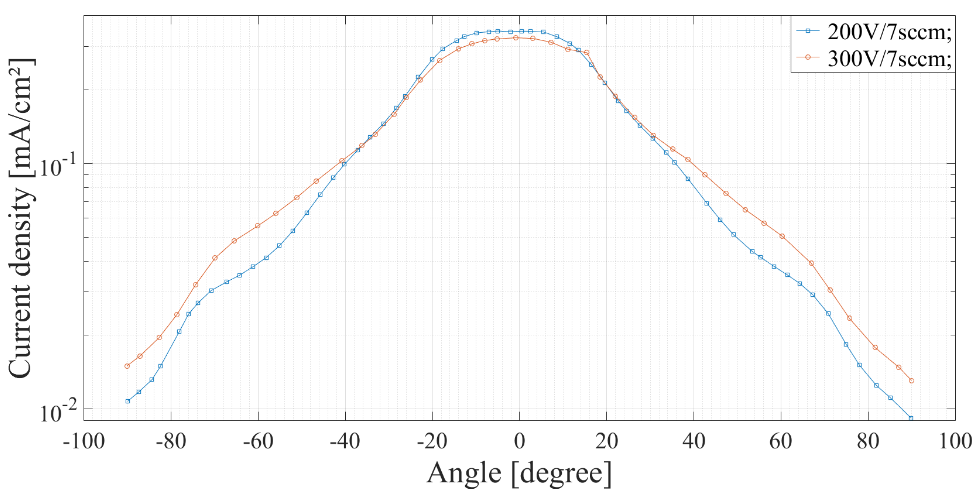

(c)

Figure 14: Ion flux measured with 4-grid RPA ("RPA X", X corresponds to the filter bias voltage with respect to ground)

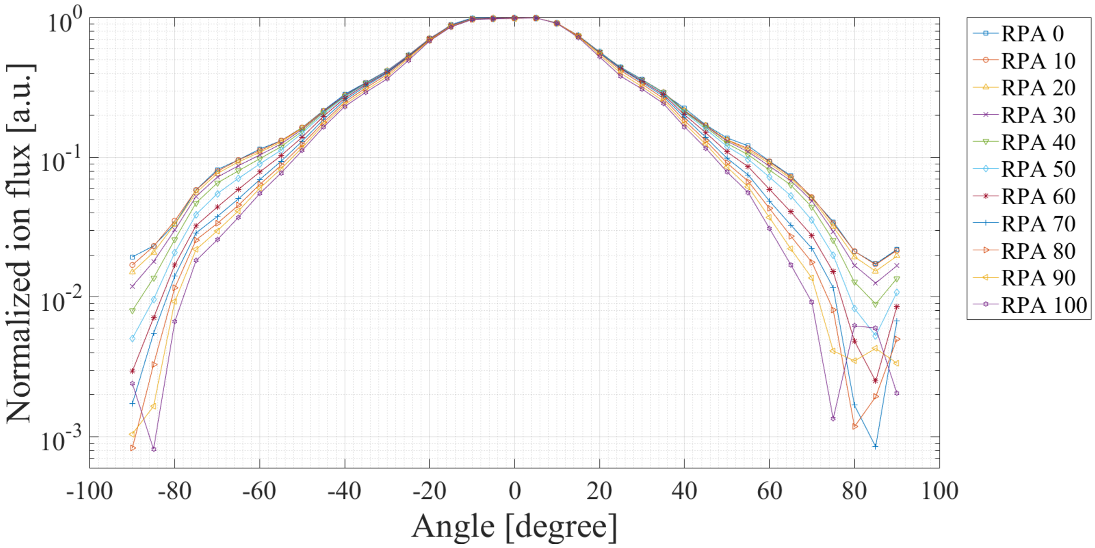

(a) 200 V, 5 SCCM

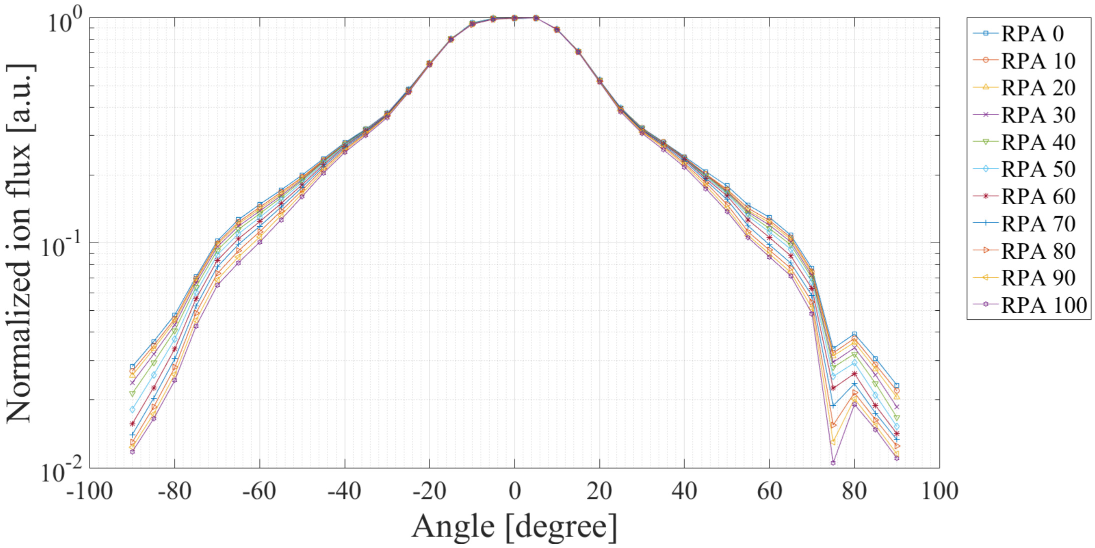

(b) 300 V, 5 SCCM

Figure 15: IEDF for low discharge voltage (200 V, 5 SCCM) at (a) 0°, (b) 20°, (c) 40°, (d) 60°, (e) 80°

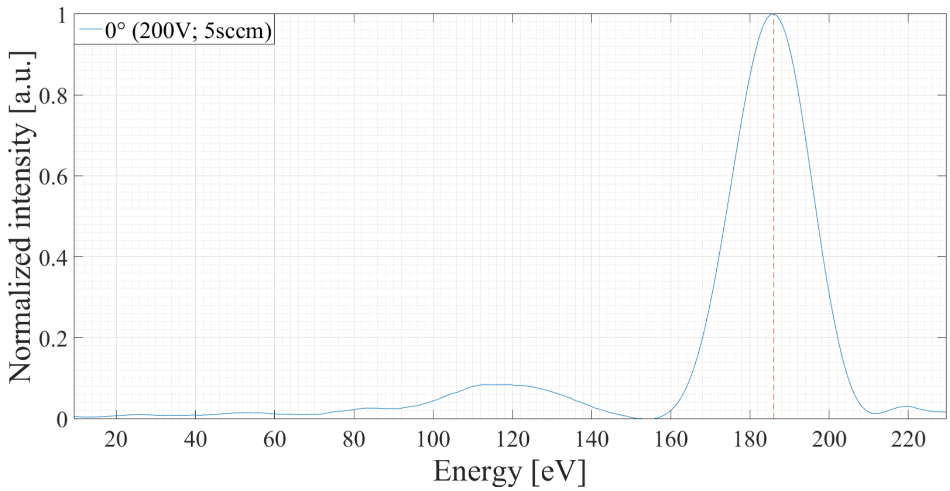

(a)

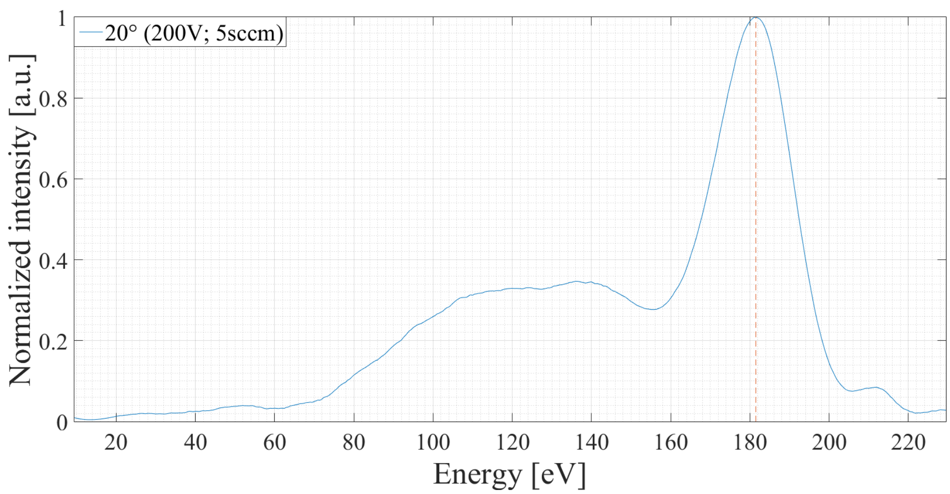

(b)

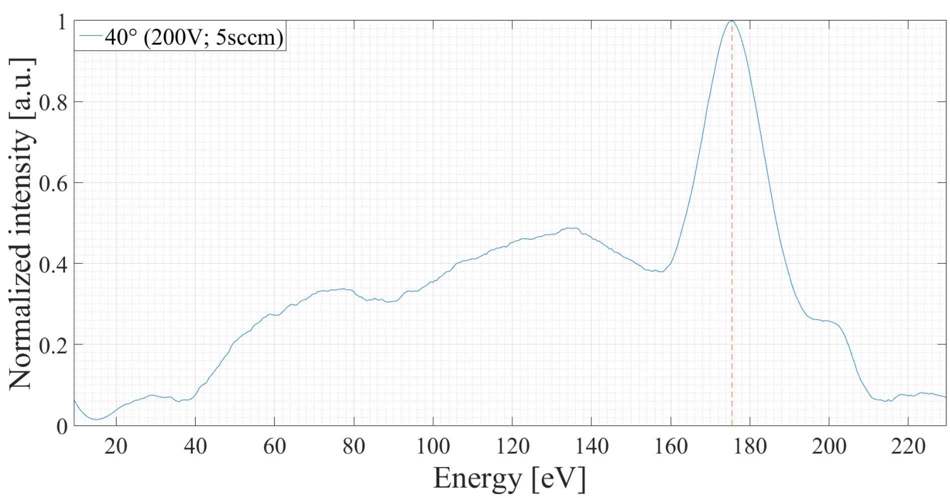

(c)

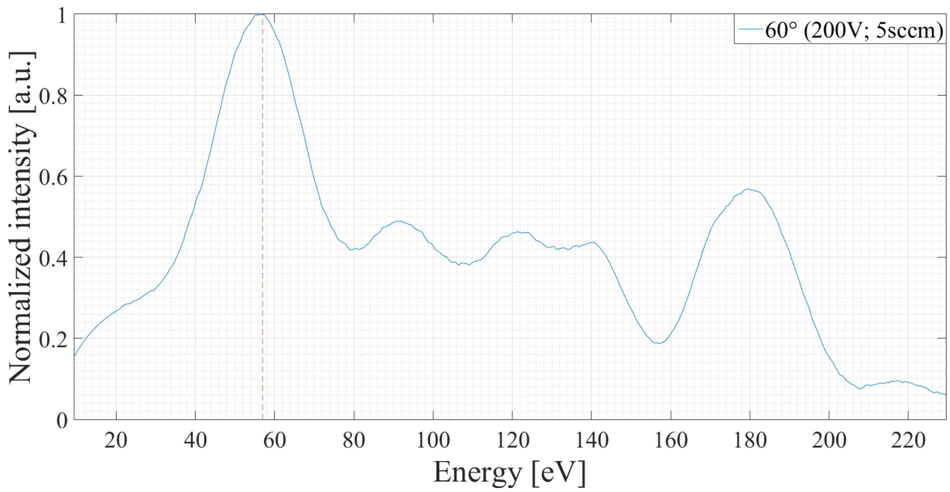
60° (200V; 5sccm)
Normalized intensity [a.u.]
Energy [eV]
0
0.2
0.4
0.6
0.8
1
20
40
60
80
100
120
140
160
180
200
220

(d)

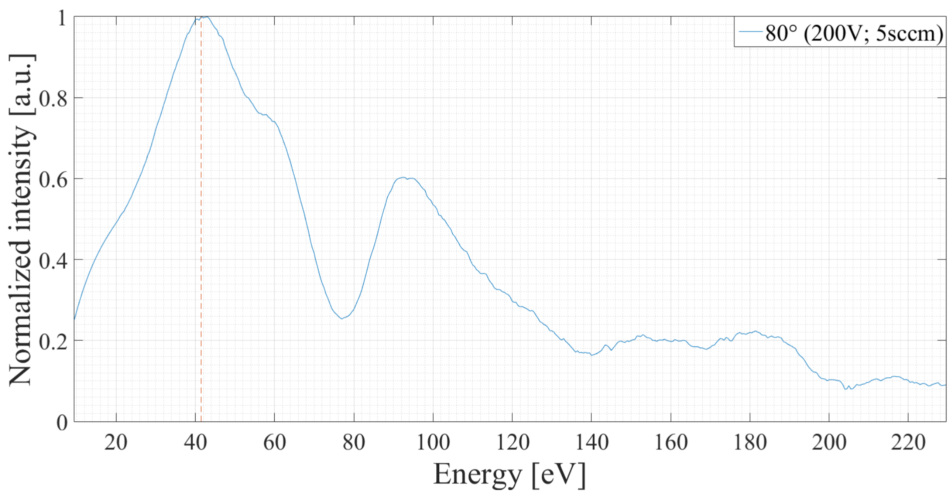
80° (200V; 5sccm)
Normalized intensity [a.u.]
Energy [eV]
0
0.2
0.4
0.6
0.8
1
20
40
60
80
100
120
140
160
180
200
220

(e)

Figure 16: IEDF for high discharge voltage (300 V, 5 SCCM) at (a) 0°, (b) 20°, (c) 40°, (d) 60°, (e) 80°

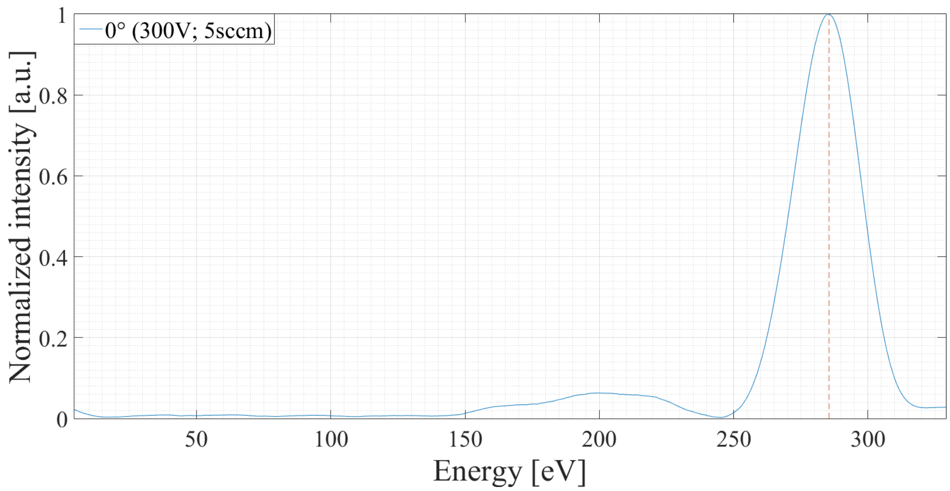

(a)

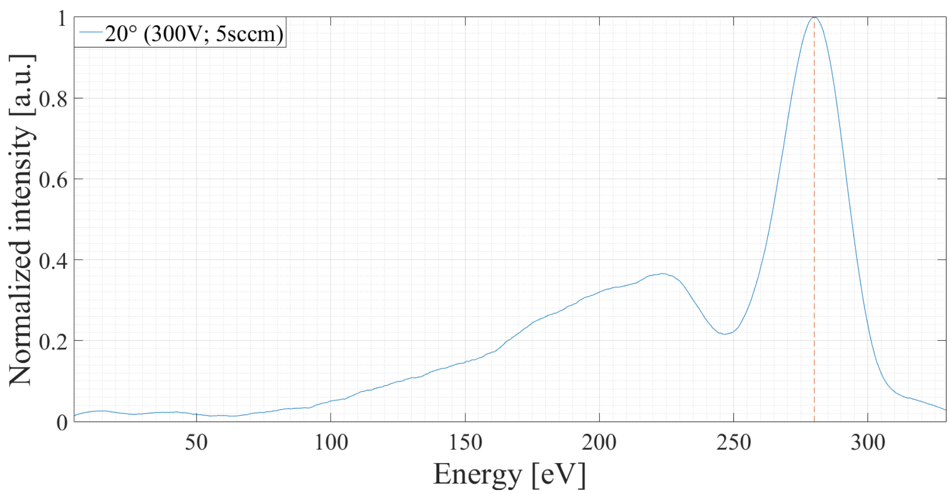

(b)

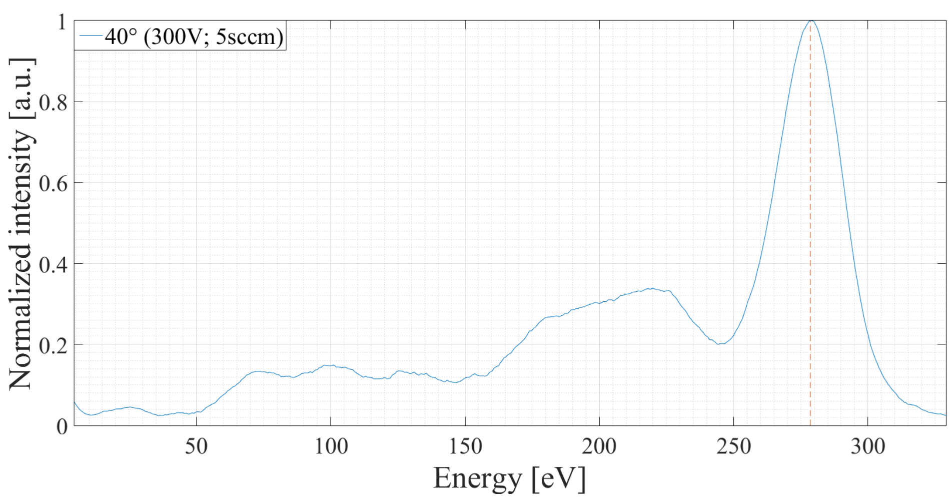

(c)

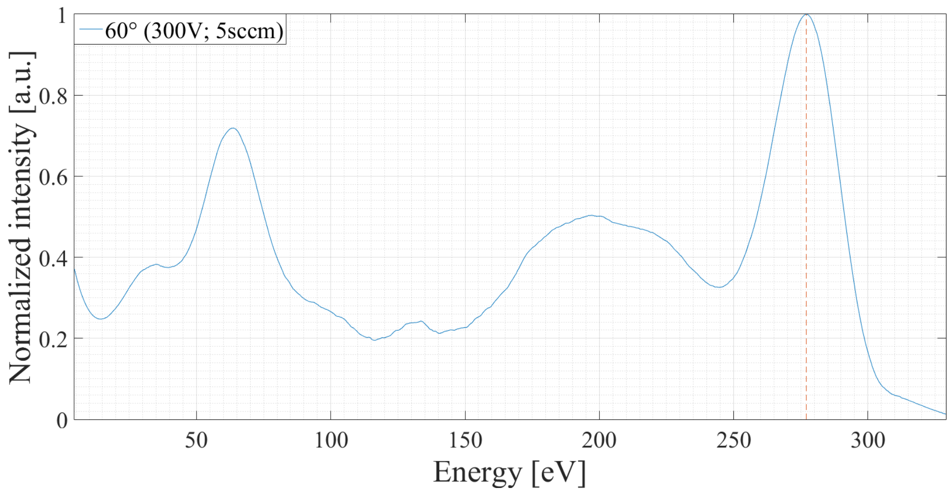
60° (300V; 5sccm)
Normalized intensity [a.u.]
Energy [eV]
0
0.2
0.4
0.6
0.8
1
50
100
150
200
250
300

(d)

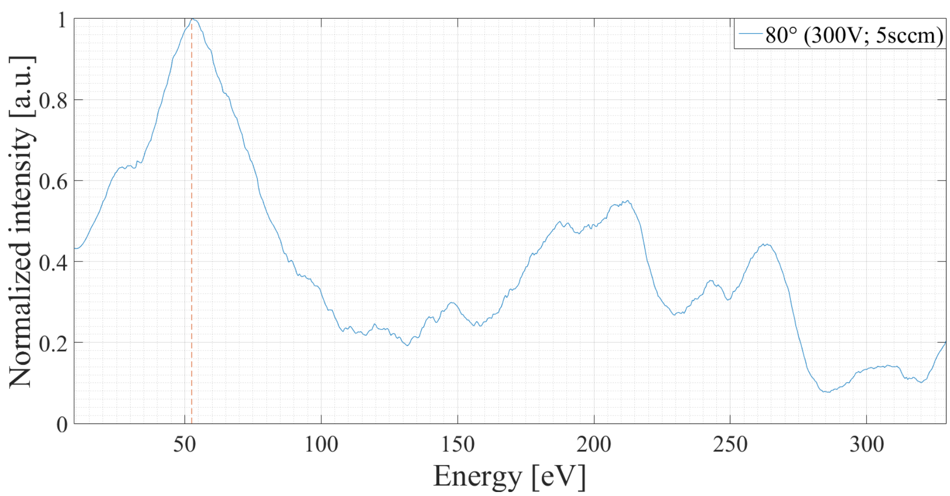
80° (300V; 5sccm)
Normalized intensity [a.u.]
Energy [eV]
0
0.2
0.4
0.6
0.8
1
50
100
150
200
250
300

(e)

Figure 17: Mean energy and most probable energy at different operating parameters

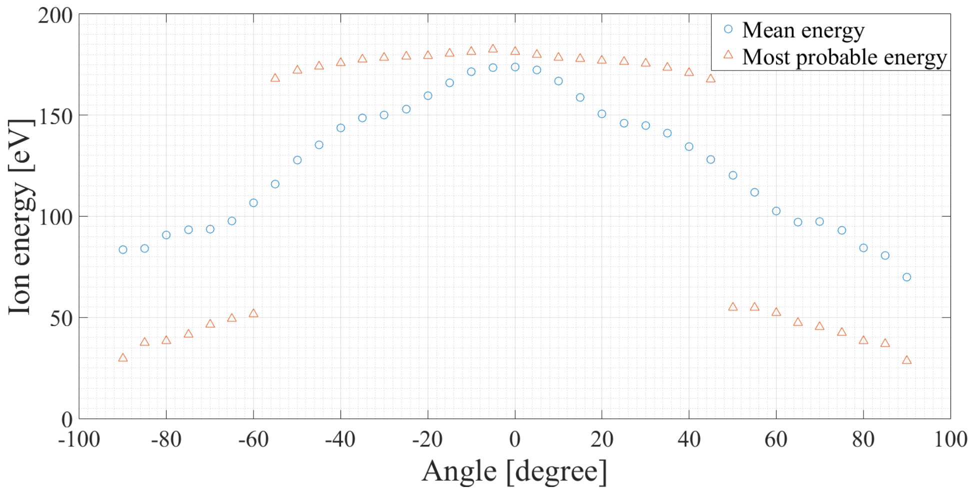

(a) 200 V, 5 SCCM

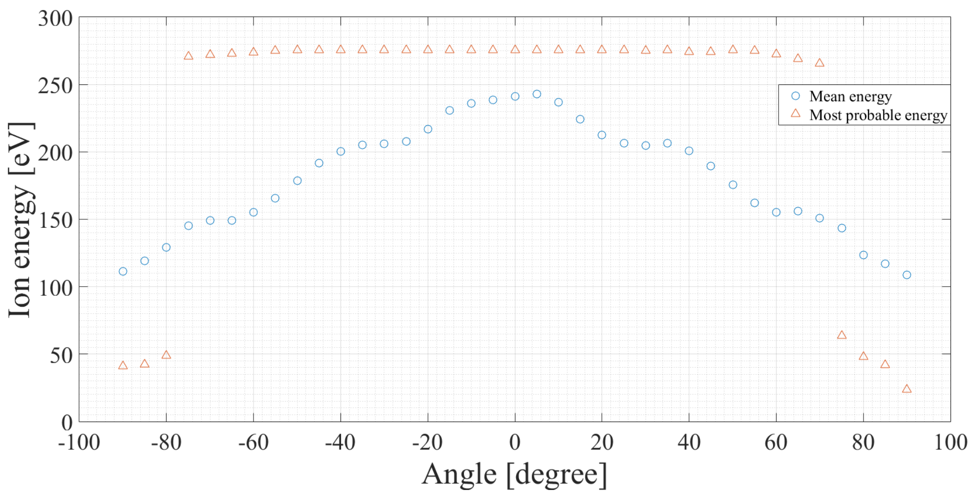

(b) 300 V, 5 SCCM

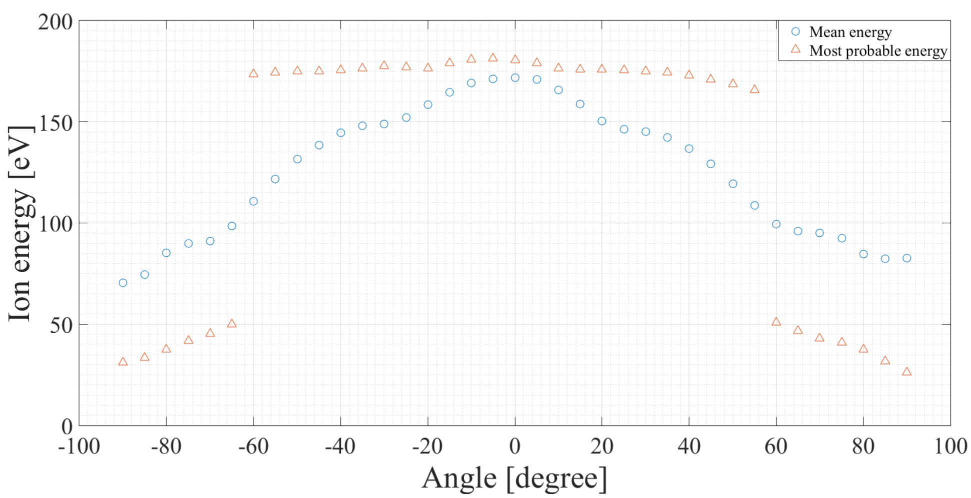

(c) 200 V, 6 SCCM

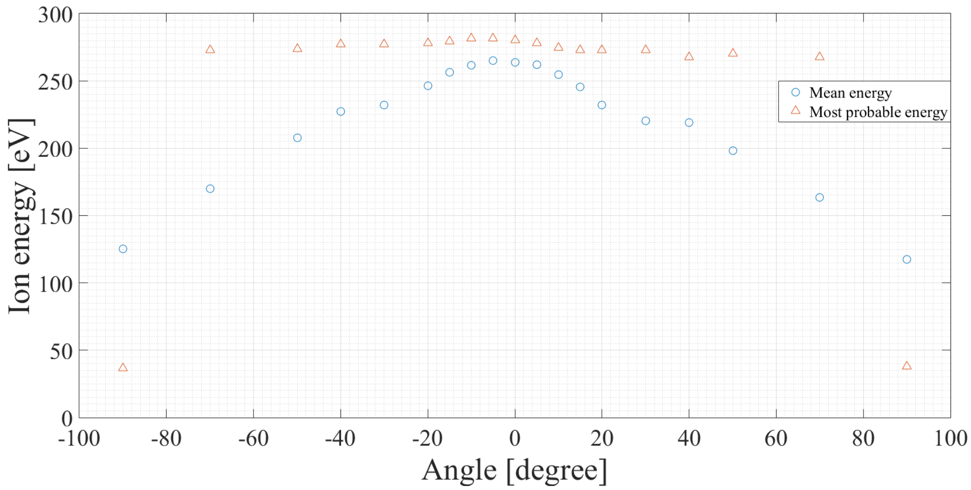

(d) 300 V, 6 SCCM

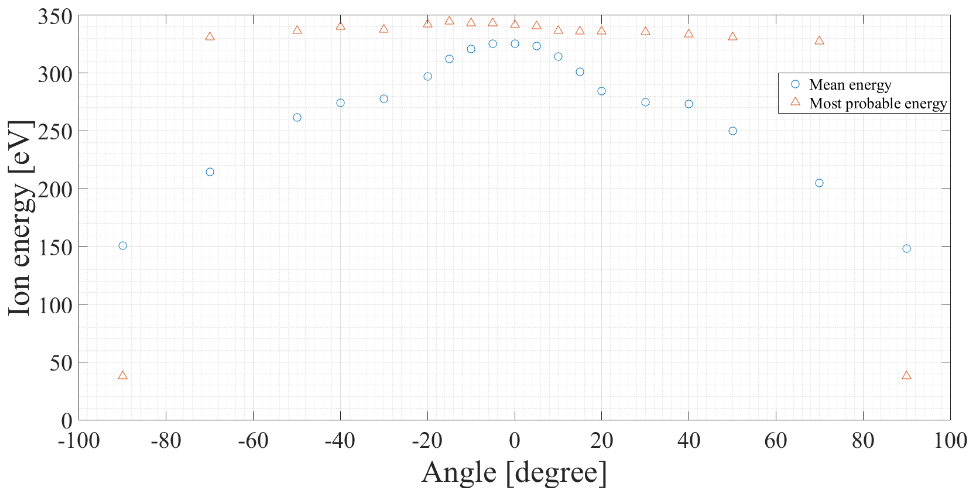

(e) 350 V, 6 SCCM

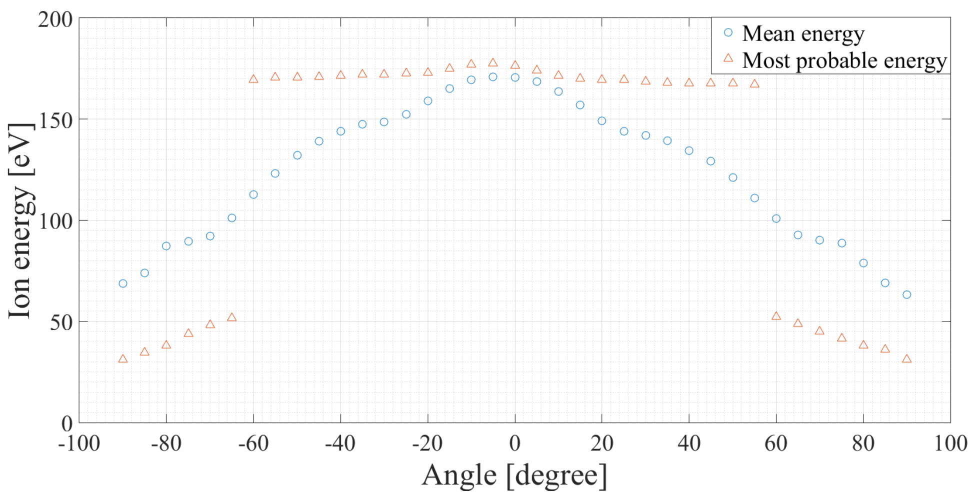

(f) 200 V, 7 SCCM

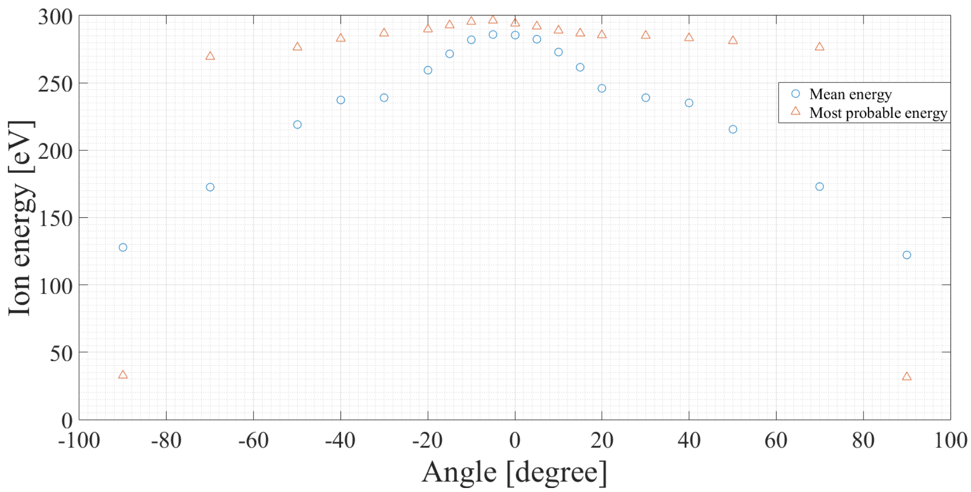
Ion energy [eV]
300
250
200
150
100
50
0
-100
-80
-60
-40
-20
0
20
40
60
80
100
Angle [degree]
Mean energy
Most probable energy

(g) 300 V, 7 SCCM

Figure 18: Contour plot of IEDF as a function of voltage

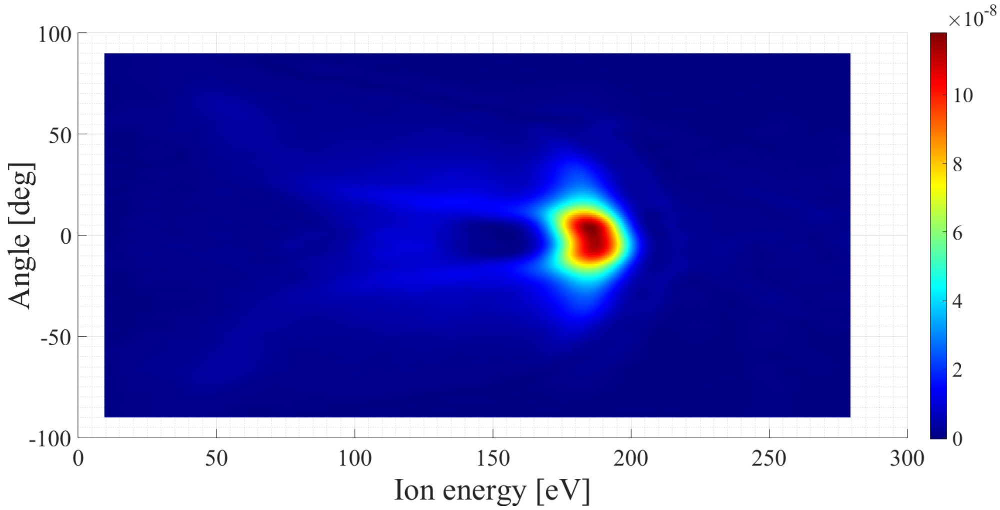

(a) 200 V, 5 SCCM

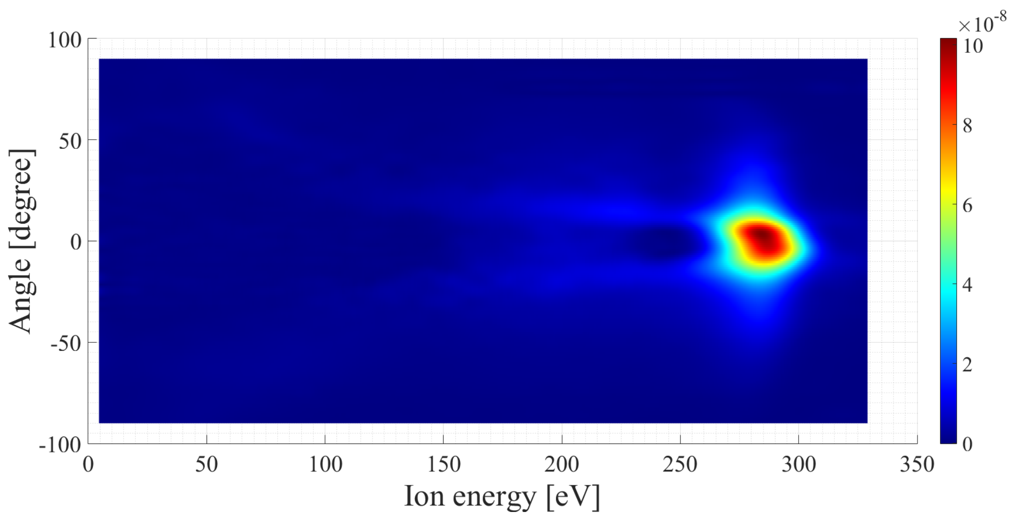

(b) 300 V, 5 SCCM

References

[1]Mazouffre, S. (2016). "Electric propulsion for satellites and spacecraft : established technologies and novel approaches". *Plasma Sources Science and Technology.*

[2]Dan M. Goebel and Ira Katz, (2008). "Fundamentals of Electric Propulsion: Ion and Hall Thrusters", *JPL Space Science and Technology Series¡*, Chap. 8

[3]Mazouffre, S., Grimaud, L. (2018). "Characteristics and Performances of a 100-W Hall Thruster for Microspacecraft". *IEEE Tansactions on Plasma Science*, 46(2), 330–337.

[4]Mazouffre, S., Largeau, G., Garrigues, L., Boniface, C., Dannenmayer, K. (2017). "Evaluation of various probe designs for measuring the ion current density in a Hall thruster plume". *35th International Electric Propulsion Conference*, IEPC-2017-336.

[5]Mazouffre, S. (2019). "Plasma diagnostic tools for ion current density and ion energy measurements". *H2020 Programm, Consortium for Hall Effect Orbital Propulsion System.*

[6]Ferda, B. (2015). "Retarding Potential Analyzer: Theory and Design", Princeton University.

[7]Fu-jun, T., Yu-xiong, X., Yi-feng, C. and al (2012). "Retarding Potential Analyzer Design and Result Analysis for Ion Energy Distribution Measurement of the Thruster Plume in the Laboratory". *International Journal of Aerospace and Mechanical Engineering*, 6(11), 2539–2542.

[8]K. Lemmer, 2009, "Use of a Helicon Source for Development of a Re-Entry Blackout Amelioration System," Ph. D. Thesis, Aerospace Engineering, University of Michigan.

[9]Vaudolon, J. (2015). "Electric field determination and magnetic topology optimization in Hall thrusters", Ph. D. Thesis, Laboratoire ICARE, Université d'Orléans.

[10] Dannenmayer, K. (2012). "Scaling laws and electron properties in Hall effect thrusters", Ph. D. Thesis, Laboratoire ICARE, Université d'Orléans.

[11]Brown, D. L., Szabo, J., and Foster, J. E. (2017). "Recommended Practice for Use of Faraday Probes in Electric Propulsion Testing", *Journal of Propulsion and Power.*

[12]Walker, M. L. R., Victor, A. L., Hofer, R. R., and Gallimore, A. D. (2005). "Effect of Backpressure on Ion Current Density Measurements in Hall Thruster Plumes", *Journal of Propulsion and Power.*

[13]Reid, B. M., Shastry, R., Gallimore, A. D., and Hofer, R. (2008). "Angularly-Resolved ExB Probe Spectra in the Plume of a 6-kW Hall Thruster". *44th AIAA/ASME/SAE/ASEE Joint Propulsion Conference and Exhibit.*

[14]Dannenmayer, K., Mazouffre, S. (2009). Elementary scaling laws for sizing up and down Hall effect thrusters : Impact of simplifying assumptions .*31st International Electric Propulsion Conference*, 1–22.

[15]King, Lyon B, Gallimore, A. D. (2004). "Ion-Energy Diagnostics in an SPT-100 Plume from Thrust Axis to Backflow". *Journal of Propulsion and Power*, 20(2).

[16]Mazouffre, S., and Kulaev, V. (2009). "Ion diagnostics of a discharge in crossed electric and magnetic fields for electric".*Plasma Sources Science and Technology.*

[17]Jared M. Ekholm, William A. Hargus and Al. (2006). "Plume Characteristics of the BHT-HD-600 Hall Thruster", *42nd AIAA/ASME/SAE/ASEE Joint Propulsion Conference.*

[18]Choueiri, E. Y. (2001). "Plasma oscillations in Hall thrusters". *Physics of Plasmas*, 8(4), 1411–1426.

[19]Gallimore, A. D. (2001). "Near- and Far-Field Characterization of Stationary Plasma Thruster Plumes Introduction". *Journal of Spacecraft and Rockets.*

[20]Gulczinski, F. S., ans Gallimore, A. D. (2001). "Near-Field Ion Energy and Species Measurements of a 5-kW Hall Thruster Introduction",*Journal of Propulsion and Power.*

[21]Kevin D. Diamant, Ty Lee, Raymond Liang and Jonathan Noland, V. V. and N. C. (2016). "Performance and Plume Characterization of the PPS ® 1350- G Hall Thruster". *52nd AIAA/SAE/ASEE Joint Propulsion Conference AIAA*, 1–16.

[22]Kevin D. Diamant, R. L. and R. L. C. (2014). "The Effect of Background Pressure on SPT-100 Hall Thruster Performance". *50th AIAA/ASME/SAE/ASEE Joint Propulsion Conference AIAA*, 1–17.

[23]Brown, D. L., Gallimore, A. D. (2009). "Evaluation of Plume Divergence and Facility Effects on Far-Field Faraday Probe Current Density Profiles". *31st International Electric Propulsion Conference.*

[24]Manzella, D. H., and Sankovic, J. M. (1995). Hall thruster ion beam characterization. *31st Joint Propulsion Conference and Exhibit.*

[25]Azziz, Y. (2007). "Experimental and Theoretical Characterization of a Hall Thruster Plume". Ph. D.Thesis, Aeronautics and Astronautics, Massachusetts Institute of Technology.

[26]Hofer, R. R. (2003). "The Influence of Current Density and Magnetic Field Topography in Optimizing the Performance , Divergence , and Plasma Oscillations of High Specific Impulse Hall Thrusters". *28th International Electric Propulsion Conference*

[27]Hofer, R. R., and Gallimore, A. D. (2006). "High-Specific Impulse Hall Thrusters , Part 2 : Efficiency Analysis". *Journal of Propulsion and Power*, 22(4).

[28] Nakles, M. R., Barry, R. R., Larson, C. W., and Hargus, W. A. (2009). "A Plume Comparison of Xenon and Krypton Propellant on a 600 W Hall Thruster". *31st International Electric Propulsion Conference*

[29]Grimaud, L. (2018). "Magnetic shielding topology applied to low power Hall thrusters". Ph. D. Thesis, Laboratoire ICARE, Université d'Orléans.